Robust Production of Parvalbumin Interneurons and Fast-Spiking Neurons from Human Medial Ganglionic Eminence Organoids

Authors: Maria C. Varela[1,2,11], Miranda P. Walker[1,2,11], Jeyoon Bok[3], Emmanuel L. Crespo[1],Tyler Thenstedt[1], Leah Goldstein[1], Andrew M. Tidball[1,2,9], Jun Z. Li[4], Yukun Yuan[5] , Lori L. Isom[1,2,5], Jianping Fu[3,6,7], Michael Uhler [2,8,9], and Jack M. Parent[1,2,9,10,12,*]

1. Department of Neurology, University of Michigan Medical School, Ann Arbor, MI, USA
2. Neuroscience Graduate Program, University of Michigan Medical School, Ann Arbor, MI, USA
3. Department of Mechanical Engineering, University of Michigan, Ann Arbor, MI, USA
4. Department of Molecular Genetics & Genome Sciences, Oklahoma University College of Medicine, Oklahoma City, OK, USA
5. Department of Pharmacology, University of Michigan Medical School, Ann Arbor, MI, USA
6. Department of Biomedical Engineering, University of Michigan, Ann Arbor, MI, USA
7. Department of Cell & Developmental Biology, University of Michigan Medical School, Ann Arbor, MI, USA
8. Department of Biological Chemistry, University of Michigan Medical School, Ann Arbor, MI, USA
9. Michigan Neuroscience Institute, University of Michigan Medical School, Ann Arbor, MI, USA
10. VA Ann Arbor Healthcare System, Ann Arbor, MI, USA
11. These authors contributed equally
12. Lead contact

*Correspondence: parent@med.umich.edu

Highlights

- Reproducible organoids highly enriched for MGE lineages
- Transcriptional and functional characterization of MGE lineage cells
- MGEOs generate major cell types and lineages of the human MGE, including robust somatostatin- and parvalbumin-expressing cortical interneurons
- MGEO-human cortical organoid assembloids display functional integration of cortical interneurons and produce complex network activity
- Fast spiking neurons are present in MGEO-cortical organoid assembloids

Summary

The medial ganglionic eminence (MGE) gives rise to parvalbumin (PV)- and somatostatin (SST)-expressing cortical interneurons essential for regulating cortical excitability. Although PV interneurons are linked to various neurodevelopmental and neurodegenerative disorders, reliably generating them from human pluripotent stem cells (hPSCs) has been extremely challenging. We present a robust, reproducible protocol for generating single-rosette MGE organoids (MGEOs) from hPSCs. Transcriptomic analyses reveal that MGEOs exhibit MGE regional identity and faithfully model the developing human fetal MGE. As MGEOs mature, they generate abundant PV-expressing cortical interneurons, including putative basket and axoaxonic cells, at a scale not previously achieved *in vitro*. When fused with hPSC-derived cortical organoids, these interneurons rapidly migrate into cortical regions, integrate into excitatory networks, and contribute to complex electrophysiological patterns and the emergence of large numbers of fast-spiking neurons. MGEOs thus offer a powerful *in vitro* approach for probing human MGE-lineage cortical and subcortical GABAergic neuron development, modeling various neuropsychiatric disorders, and advancing cell-based therapies for neurodevelopmental and neurodegenerative disorders.

Graphical abstract

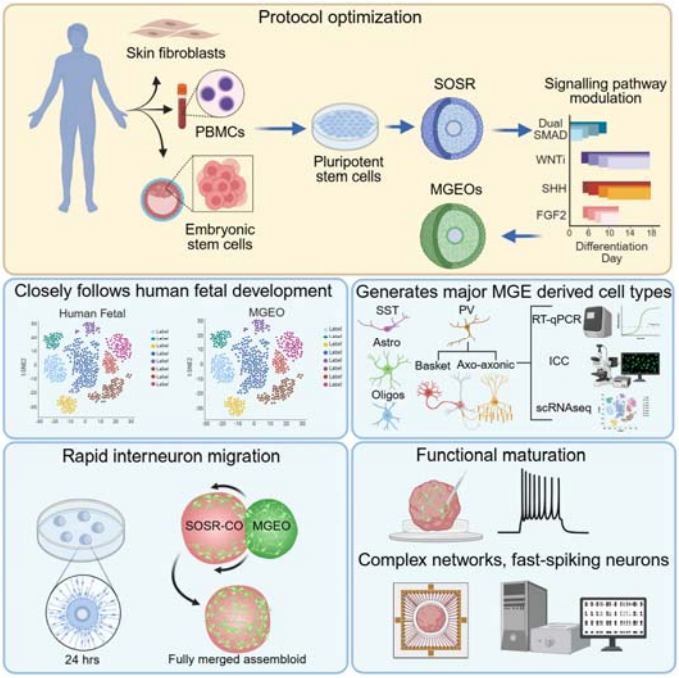

Keywords

GABAergic · brain organoid · pluripotent stem cells · neuronal migration · forebrain development · multielectrode array · basket cells · axoaxonic cells

INTRODUCTION

The developing human cortex is largely populated by two divergent classes of neurons: glutamatergic excitatory neurons and gamma-aminobutyric acid (GABA)-containing inhibitory interneurons. Glutamatergic neurons are generated in the dorsal telencephalon and migrate radially as they form the cortical layers. In contrast, the majority of pallial GABAergic interneurons are generated in the ganglionic eminences (GEs) before migrating tangentially to the basal telencephalon. These neurons are essential for maintaining the balance of excitation and inhibition within neural circuits, which is fundamental for proper neural circuit function and cortical information processing[1]. GABAergic neurons precisely modulate brain network activity by regulating the timing and synchrony of neuronal firing, leading to the formation of neuronal oscillations critical for information transfer in the brain[2–4]. Disruptions in the migration, maturation, synaptogenesis or function of these interneurons have been linked to various neurologic and psychiatric disorders. These disorders include

neurodevelopmental conditions[5], such as autism[6–11], attention deficit disorder and intellectual disability[12,13], epilepsy[14–18], and schizophrenia[19–21], as well as neurodegenerative diseases[22], highlighting the critical nature of these cells in maintaining neural homeostasis.

The GEs are transient structures in the developing brain comprised of three distinct regions: medial ganglionic eminence (MGE), caudal ganglionic eminence (CGE) and lateral ganglionic eminence (LGE). The MGE and CGE, along with the preoptic area (POA), generate the majority of interneurons in the cortex and hippocampus. The MGE serves as the origin of approximately 60% of cortical interneurons and produces several interneuron subtypes crucial for cortical function[23–28]. The MGE is characterized by the expression of the forebrain marker FOXG1, as well as homeobox transcription factors NKX2.1 and LHX6, with no expression of the dorsal cortical marker PAX6 or the more ventral hypothalamic marker RAX[29–33].

NKX2.1 is not specific to the MGE as it is also expressed in the rostral pallidum, ventral septum, preoptic area, and ventral hypothalamic regions. In contrast, *LHX6* is largely restricted to MGE-derived lineages. In most human MGE-derived GABAergic lineages, upregulation of *LHX6* is induced by *NKX2.1* expression at approximtely gestational week 8 (GW8) in humans or embryonic day 11.5 in mice and is essential for the proper positioning and maturation of cortical SST and PV interneurons [24,25,34–41]. In addition to SST and PV cortical interneurons, the MGE also produces GABAergic and cholinergic striatal interneurons, subpallial GABAergic projection neurons, astrocytes, and oligodendrocytes[38,42,43].

Recent transcriptomic studies of human fetal brain tissues have provided significant insights into the gene expression profiles of the developing human GEs[29,32,33,44,45]. However, the availability of human brain tissues from a broad range of fetal development is limited. To address this limitation, human pluripotent stem cell (hPSC)-derived 2D and brain organoid models have emerged as promising tools for recapitulating neural development *in vitro*. In particular, brain organoids are 3D

structures that recapitulate key aspects of brain cytoarchitecture, cellular diversity, and complex network connectivity. These models simulate key features of the native brain environment and offer the potential for generating unique insights into human neurodevelopment and associated disorders.

Several pioneering methods have generated GABAergic neurons from hPSCs in both 2D cultures[30,31,46] and 3D brain organoid models[47–50]. These methods produce NKX2.1+ progenitors and generate primarily GABAergic SST+ neurons and neurons that arise from other subpallial regions but little to no PV+ cortical interneurons in culture. PV+ interneurons are the largest class of interneurons in the human cortex, comprising approximately 30-40% of all cortical interneurons, and play a critical role in regulating cortical excitability. PV interneuron fast-spiking properties allow them to tightly regulate and synchronize cortical network activity through gamma oscillations. These oscillations facilitate rapid information transfer across brain circuits and thus are critical for cognition, sensory processing, and working memory. Dysregulation of PV interneuron development and function is implicated in epilepsy, schizophrenia, and autism spectrum disorders, making them a highly desirable cell type to generate for *in vitro* disease modeling[11,15,51,52]. To date, however, no hPSC-derived *in vitro* model has been reported that consistently and robustly generates PV cortical interneurons or fast-spiking neurons.

Here we describe a human MGE-specific organoid (MGEO) model that exhibits MGE lineage marker expression and cell type specificity. The model exhibits transcriptomic similarities to human fetal MGE, generates highly migratory pallial interneuron progenitors, and displays robust development of MGE lineage interneuron subtypes that include SST and PV interneurons. When fused to human cortical organoids (hCOs) to generate assembloids, MGEO-derived interneurons migrate into hCOs where they integrate with excitatory cortical neurons, leading to complex network activity and the development of fast-spiking neurons. Our model offers a powerful platform for studying human-specific MGE interneuron development and disorders related to MGE

interneuron dysfunction and provides a potential source of MGE interneuron progenitors for therapeutic grafting.

RESULTS

Timing and concentration of patterning molecules influence MGE specificity of subpallial organoids.

Regional specification of the MGE is mediated by precisely controlled spatiotemporal signals, including gradients of Wingless-related Integration Site (WNT) and Sonic Hedgehog (SHH), during forebrain development (**Figure 1A**)[53,54]. In addition to the notochord, SHH is also expressed at high levels in the preoptic area (POA) and floor plate, while its expression is present to a lesser extent in the MGE[55–57]. Conversely, WNT expression is highest in the cortex with a graduated decrease in expression in ventral telencephalic regions[53,54]. Established protocols for generating ventral telencephalic (subpallial) organoids rely on SHH pathway agonists and WNT pathway antagonists to guide organoids towards a ventral brain region identity [47,48,50].

We recently developed a method for generating dorsal forebrain patterned self-organizing single-rosette cortical organoids, termed SOSR-COs[58]. Given the robust cell-type specificity, reproducibility, and improved structural organization of the single-rosette organoids for modeling early neurodevelopmental disorders,[58–60] we used this approach as a foundation for developing self-organizing single rosette MGE organoids (MGEOs), with the aim of achieving MGE regional specificity with a high yield of PV+ cortical interneurons. Unlike multi-rosette protocols that begin with aggregation of hPSCs into embryoid bodies, the MGEO protocol starts from modeling the formation of the neural plate by first culturing a 2D monolayer of hPSCs and exposing them to dual SMAD inhibition. The monolayer is then cut into evenly sized squares and plated onto thick extracellular matrix (100% Geltrex), allowing each piece to self-organize into a single rosette structure which is subsequently removed from the matrix and grown in suspension[58].

In our initial attempt to create single rosette subpallial organoids, we exposed organoids to smoothened agonist (SAG;1 μM) to activate the SHH signaling pathway and the WNT pathway antagonist XAV939 (2 μM) from days *in vitro* (DIV) 6 to 14 based on existing subpallial organoid protocols[48,61,62] **(Figure S1A**). This morphogen patterning protocol produced organoids that lacked MGE regional specificity, as assessed by single-cell RNA-sequencing (scRNA-seq) of 1-month old organoids (**Figure S1B-D**)**.** This regionally mixed population of cells included clusters of GE-derived neurons, POMC+ hypothalamic neurons, probable glutamatergic early-born cortical neurons, and neurons with a midbrain/hindbrain identity. Neurons expressing SHH, RAX (hypothalamus marker), and the preoptic area marker HMX3 were also evident (**Figure S1D**). Notably, although we found a large population of NKX2.1 expressing cells, minimal expression of markers for forebrain (FOXG1), MGE (LHX6), or the PV precursor marker MEF2C was detected in these cells (**Figure S1D**). These results were similar to findings from other subpallial organoid protocols that contain a mixture of CGE, LGE, MGE and other regional identities, with absent or minimal expression of the MGE marker LHX6 or PV cortical interneurons [48,61,65,79].

To increase the MGE specificity of our model, we next systematically altered the timing of dual SMAD inhibition, as well as the timing and concentrations of SAG and XAV939 (**Figure 1B**). We quantified expression of region-specific mRNAs at 18 DIV using RT-qPCR (**Figure 1C**) and found that *PAX6*, a dorsal telencephalic marker with some expression in LGE and CGE, but not MGE[63], was more highly expressed in conditions with earlier SAG exposure, while *LHX6* was more highly expressed with later SAG exposure. Conditions with higher SAG concentrations resulted in higher levels of *SHH* mRNA expression, suggesting subpallial organoids with a regional identity associated with deeper ventral telencephalic regions including the preoptic area (POA) and hypothalamus[53]. In contrast, *NKX2.1* was expressed at relatively similar levels across all conditions, demonstrating that *NKX2.1* expression alone cannot be used as a sole marker to establish MGE identity. A combination of 100 nM SAG exposure from 10-18 DIV, brief XAV939 exposure during SMAD inhibition, and FGF2 treatment from 6-12 DIV showed the greatest MGE-like specificity as defined by high *LHX6* expression,

moderate *NKX2.1* expression, and negligible levels of *PAX6* and *RAX* expression(**Figure 1C,** bottom row). We therefore selected this specific patterning protocol for generating MGEOs for the rest of this study (**Figure 1D**).

MGEOs display high MGE regional specificity

To ensure the robustness of our protocol across different cell lines, we conducted our experiments using human foreskin fibroblast- and blood-derived iPSC lines, denoted as 2E and 79B, respectively, as well as a human embryonic stem cell (hESC) line (H9). Continuing WNT inhibition until 10 DIV followed by SHH pathway activation from days 10 to 18 consistently produced MGEOs with robust expression of key forebrain-specific (*FOXG1*), ganglionic eminence progenitor (*NKX2.1*), and MGE-specific (*LHX6*) markers for all the hPSC lines, as measured by RT-qPCR at one, two, and three months (**Figure 1E, F**)[64,66]. LHX6 mRNA and protein remained highly expressed in MGEOs from 1 to 3 months **(Figure 1E, F)**. Negligible mRNA expression levels of the hypothalamic marker RAX and the dorsal telencephalic marker *PAX6* were observed **(Figure 1E)**, with only miniscule amounts in glial clusters of our scRNA-seq analyses **(Figures 2 & 4**), but no protein expression observed by immunostaining for PAX6 or RAX in 1-month MGEOs (**Figure S2A-C**). Immunostaining of MGEOs at 1 and 3 months also supported the MGE specificity, with high expression of GABA, LHX6, NXK2.1, and OLIG2 (**Figure 1F**).

To further validate the MGE specificity of our organoids, colocalized expression of OLIG2 and NKX2.1 was quantified through immunofluorescence analysis. In early developmental timepoints of the human brain (GW 8-12), OLIG2 expression almost exclusively colocalizes with expression of NKX2.1 in the MGE but not in surrounding brain regions including the LGE, CGE, hypothalamus, and preoptic areas[31,44]. At mid to late gestational weeks (GW 24+), NKX2.1 and OLIG2 segregate in their expression patterns and do not co-express in mature MGE-derived cells. Our analysis of 1-month MGEOs shows a 98.5% colocalization of OLIG2+ cells with NKX2.1 (**Figure S2D, E**). In 3-month MGEOs, in contrast, most OLIG2+ cells did not colocalize with NKX2.1 (**Figure S2D, E**). These results further support the MGE specificity of our model.

Newborn cortical interneurons express ERBB4, which is required for their tangential migration[67]. Migratory MGE cortical interneurons are distinguished from other GABAergic lineages by the co-expression of *LHX6*, *MAF*, and *MAFB*, alongside downregulated *NKX2.1* and *LHX8*. In contrast, subpallial lineages (GABAergic and cholinergic neurons) maintain the expression of *LHX8* and *NKX2.1* and do not express *MAF* genes[29,33]. Single-cell RNA-sequencing (scRNA-seq) analysis of 1-month MGEOs with Uniform Manifold Approximation and Projections (UMAP) plots revealed five distinct cell clusters annotated as radial glia (*VIM, NES, HES1*), inhibitory neuron progenitors (*ASCL1, HES6, DLX2*), and populations of GABAergic neurons that resemble tangentially migrating somatostatin (*SST*)+ cortical interneurons (*SST, LHX6, CXCR4, ERBB4, ZEB2, PLS3, ARX, MAF*), PV neuron precursors (*MAFB, MEF2C, ETV1, ST18, CRABP1*), and MGE subpallial destined neurons (*LHX8, GBX2*)[29,32,33,45] (**Figure 2A**). Importantly, the percent distribution of each of these cell types in MGEOs was consistent within each sample replicate and between hPSC lines (**Figure 2B**). We confirmed the presence of cells in MGEOs expressing the MGE-specific marker LHX6, as well as the absence of cells expressing off target markers that would indicate non-MGE identities, including CGE (*SP8, COUPTF2(NR2F2)*), LGE (*EBF1, ZFHX3*), hypothalamus (*NKX2-2, RAX*), POA (*HMX3, DBH*) and dorsal telencephalon (*PAX6*) (**Figure 2C,D**). Together these data strongly support the MGE specificity of MGEOs.

MGEOs produce human MGE-derived cell types

To characterize the cell types produced in MGEOs, we conducted RT-qPCR and scRNAseq analysis for MGEOs at 3 months, and immunostaining from 3-8 months. The MGE primarily generates SST and PV GABAergic neuron subtypes, although there is evidence that to a lesser extent it generates neurons that express calretinin (*CALB2*), TH, and CHAT[24,64,68,69]. The MGE also gives rise to astrocytes and oligodendrocytes[70,71]. Our RT-qPCR analysis of MGEOs (**Figure 3A**) revealed that the GABAergic neuronal markers VGAT and SST were expressed in MGEOs generated from all three hPSC lines at one, two, and three months. Expression of *SLC12A5* (KCC2) relative to *SLC32A2* (NKCC1) progressively increased from one month to three months, consistent with interneuron maturation. As expected, *LHX8* expression was

highly upregulated in MGEOs at 1 month and decreased thereafter. While calretinin interneurons primarily originate from the CGE, a subpopulation of calretinin interneurons is known to arise from the dorsal MGE[23,24,35,72]. We identified populations of calretinin (CR) and SST expressing neurons, both of which also expressed *LHX6*, indicating that both populations were derived from an MGE-like lineage (**Figure 3B, C**). Immunostaining of MGEOs at 3 months also revealed expression of GFAP in putative astrocytes, and sparse oligodendrocytes expressing both myelin basic protein (MBP) and OLIG2 (**Figure 3D**).

In 1- and 3-month MGEOs, RT-qPCR and immunostaining showed robust expression of MEF2C (**Figure 3A, G, H)**, an early marker of PV-fated cortical interneurons[73,74]. Immunostaining analysis of 3-month MGEOs further revealed a small number of PV-immunoreactive cells (2.2% ± 0.63 of DAPI area, **Figure 3E, F**). At 4 months, however, PV immunolabeling robustly increased (32.8% ±7.52) and was maintained at 6 (31.3% ± 7.06) and 8 months (32.5% ± 5.75) (**Figure 3E,F**). PV fast-spiking cortical interneurons express K_v3 family potassium channels, predominantly $K_v3.1$ and $K_v3.2$[75]. Although expression of *KCNC1*, which encodes $K_v3.1$, was already present in 1-month MGEOs (**Figure 3A**), there was minimal $K_v3.1$ immunolabeling in 3-month MGEOs **(Figure 3H**), similar to PV immunoreactivity at this time point. However, $K_v3.1$ immunolabeling increased markedly in 8-month MGEOs and was seen predominantly in MEF2C+ cells (**Figure 3H**). In 6-month MGEOs, we observed PV-immunoreactive cells co-expressing Wisteria floribunda agglutinin (WFA), a marker for perineuronal nets that surround fast-spiking interneurons (**Figure 3I**)[76,77]. Viral labeling using an AAV1 PV basket cell-specific enhancer-driven tdTomato virus (AAV1-BiPVe3-dTom)[78] confirmed the presence of putative PV basket cells with complex morphologies in 6-month MGEOs (**Figure 3J**). Together, these data indicate that MGEOs robustly produce PV+ cortical interneurons within 4 months in culture that exhibit molecular and structural features consistent with fast-spiking activity.

Analysis of scRNA-seq data from 3-month MGEOs generated from all the three hPSC lines revealed distinct MGE-like cell lineages including: cortical PV precursors with or

without CRAPBP1, SST+ cortical-destined cells, and MGE subpallial/striatal/globus pallidus-destined cells with or without *LHX8* expression (**Figure 4A, C, D**). Additionally, the presence of astrocytes/pre-astrocytes and pre-oligodendrocyte precursor cells (pre-OPCs)/OPCs in the MGEOs were identified (**Figure 4A, right side**). While there was some variation in the cellular composition between experimental replicates and MGEOs generated from different hPSC lines (**Figure 4A**), the average percentages of GABAergic precursors/neurons, pre-astrocytes/astrocytes, pre-OPCs/OPCs, and dividing cells were highly consistent between cell lines and replicates (**Figure 4B**). As expected, there was negligible expression of the CGE lineage GABAergic neuron subtypes *VIP* (**Figure S3A,C),** or *CCK* (**Figures 4C**, **S3C**) in 3-month MGEOs. Expression of *NPY* in 3-month MGEOs was limited to *SST*+/ *NPY*+ cortical-destined neurons (**Figure 4A-C**). *CALB2*+ (calretinin) cells were found in the striatal/GP-destined clusters and co-expressed *NKX2.1,* as well as in the cortical destined clusters that co-expressed *LHX6* (**Figure 4A,C; Figure S3**). Neither of these populations showed upregulated expression of CGE markers *SP8* or *NR2F2* (*COUPTFII*) **(Figure S3B**), supporting their non-CGE origin. Consistent with our previous findings, there was minimal off-target region-specific marker expression (**Figure 4C,D; Figure S3C**).

In comparing the percentage of GABAergic neuron subtypes present in 3-month MGEOs with those in human MGE fetal and subpallial organoid datasets[29,61,79], we found that the MGEOs produced much larger percentages of GABAergic neurons and MGE-specific GABAergic neuron subtypes (**Figure S3C**)), likely because many of these cells migrated to the cortex or basal ganglia in the fetal brain but remained present in the MGEOs. Additionally, several cell populations in 3-month MGEOs expressed markers of cortical PV precursors, including *LHX6, MEF2C, MAFB, ERBB4, ETV1*, or markers of subpallial destined PV precursors, with co-expression of LHX8, TAC1, and CRABP1(**Figure S3D**). Detailed analyses of gene expression patterns of GABAergic neuron subtypes in the MGEOs further revealed that many cells co-expressed *SST*, including *SST+/CHODL*+, *SST+/CALB2*+, and *SST*+/*NPY*+ combinations, known *SST* subtypes generated in the MGE[80,81]. Notably, *SST, CHODL, CALB2*, and *NPY* were largely not co-expressed in PV+ (*PVALB*) cells, consistent with

prior studies showing that PV$^+$ and SST$^+$ interneurons, though both derived from the MGE, represent virtually non-overlapping cell populations[82] (**Figure S3E)**. Together these results suggest that MGEOs produce cell types that are predominantly specific to an *in vivo* MGE regional identity.

MGEO transcriptome closely resembles that of the developing human MGE

To assess the fidelity of the MGEO model in recapitulating the transcriptomic features of the developing human MGE, we compared the scRNAseq data of 90 DIV MGEOs to a human fetal GE scRNA-seq dataset published by Shi and colleagues[29]. The human fetal GE dataset was visualized by UMAP plot using cell cluster annotations originally assigned in the dataset and then integrated with our MGEO dataset, and the relationships analyzed using UMAP and PCA plots (**Figure 5A-D**). The resulting plots demonstrated a close overlap of MGEOs with the human fetal MGE cluster, suggesting that the transcriptome of the organoids closely mirrors that of the human fetal MGE.

We next conducted Pearson correlation analysis to compare the neuronal clusters in the MGEOs with the human MGE cell lineage clusters from the human fetal GE dataset. A high degree of similarity between the corresponding neuronal subtypes in both datasets was revealed (**Figure 5E**), reinforcing the fidelity of the MGEO model to the human MGE.

We then compared gene expression between the MGEOs, human MGE, and two published subpallial organoid models[29,49,50] by analyzing the percentage of cells expressing genes specific to various regions of the developing subpallium (**Figure 5F**). The results demonstrated that MGEOs exhibit strong expression of MGE-specific markers, with minimal off-target expression of genes associated with other brain regions including LGE, CGE, POA, and hypothalamus. In contrast, other subpallial organoids[61,62] showed a broader distribution of gene expression, with regionally mixed expression patterns and very limited MGE specificity.

Importantly, integration of MGEO data from multiple cell lines with human data across various gestational weeks showed that MGEOs consistently clustered within the MGE region across all datasets, demonstrating that the model is robust across different cell lines (**Figure 5B, G**). A UMAP plot of the 3-month MGEO clusters mapped onto the integrated human dataset revealed that the cell types within the MGEOs closely align with those of the human MGE at similar stages of development (**Figure 5G**). To further investigate the developmental trajectory of the MGEOs, we computed Euclidean distances between MGEOs and the human dataset[29] at different gestational weeks (**Figure 5H**). The heatmap revealed that the 3-month MGEOs most closely resemble human MGE tissue from gestational weeks 12-16. Together, these data show that the MGEO model captures key features of MGE cellular diversity and accurately recapitulates the transcriptomic signature of the developing human MGE.

MGEOs recapitulate cortical interneuron migration and structural integration in assembloids

Given that MGE-derived cortical interneurons are highly migratory and possess specific migratory characteristics that differentiate them from radially migrating cortical neurons[83,84], we next characterized migratory properties of interneuron progenitors in MGEOs alone and in assembloids after fusion with COs. MGEOs at different time points were first plated on extracellular matrix (ECM)-coated plates (**Figure 6A).** Day 21 was the earliest time in which neuron-specific migration could be observed without the spread of proliferative cells (**Figure 6B-C**). Specifically, robust migration of neuronal cells onto the 2D ECM and away from the MGEO was observed beginning at 2-4 hours post plating of day 21 MGEOs. Neuronal migration was rapid, as seen by comparing images at 0-, 12- and 24-hours post-plating of the MGEOs (**Figure 6B', Video S1**). Importantly, cells that migrated away from the MGEOs co-expressed MAP2ab and LHX6, supporting their neuronal and MGE lineage identity (**Figure 6C**).

Cortical interneurons migrate tangentially from subpallial regions to the cortex and are directionally guided by attractive and repulsive cues expressed in the cortex, striatum, and globus pallidus[85,86] For example, binding of the α-chemokine SDF-1 (CXCL12) to

the G-protein-coupled CXCR4 receptor in migrating interneurons facilities tangential migration (**Figure S4A**)[87,88]. Strong expression of *CXCR4*, *SDF-1*, and *CXCR7*, another chemokine receptor involved in interneuron migration, was observed in the 1-month MGEO scRNA-seq dataset (**Figure S4B**). Next, we plated MGEOs on Geltrex at day 30 and assayed for cell migration over 2 days while exposing them to 100 nM of the CXCR4 inhibitor AMD3100 for 8 days (Chronic; 6 days before and 2 days after plating) or 2 days (Acute; after plating) (**Figure S4C**). We measured the area of migrated neurons outside the organoids at 48 hours post plating. Although the average migrated neuron area from MGEOs in the Acute treatment group was not statistically different from vehicle-treated controls ($p = 0.113$), MGEOs chronically treated with AMD3100 showed significantly reduced neuronal migration vs control ($p = 0.0036$) (**Figure S4D,E**). The reduced migration of MGEO-derived putative interneurons with CXCR4 antagonist treatment suggests that, similar to *in vivo* mechanisms, cortical interneuron migration from MGEOs is influenced by SDF-1/CXCR4 interactions.

To further validate migration of interneurons developed in MGEOs using an assay that more faithfully recapitulates *in vivo* cortical interneuron migration, we fused MGEOs with dorsally patterned SOSR-COs (hereafter referred to as “CO”)[58] at 56-58 DIV to generate assembloids. Prior to fusion, MGEOs and COs were virally labeled with mDLX-GFP[89], and CAG-tdTomato, respectively (**Figure 6D**). We observed robust migration of mDLX-GFP+ interneurons that began several hours after fusion and continued rapidly throughout the first two weeks post-fusion (**Figure 6E-G, Video S2)**. The rapid migration of mDLX-GFP+ interneurons was consistent across cell lines and experimental replicates (**Figure 6G**). Migrating interneurons displayed properties indicative of cortical interneuron migration, including somal translocation and leading-edge branching in MGEO-CO assembloids **(Figure 6H, Video S3**) as well as in 2D assays described above (**Video S1**). Notably, MGEO-CO fusions treated with AMD3100 1-day post fusion trended toward reduced mDLX-GFP+ interneuron migration into the COs versus controls after 24-hour AMD3100 treatment ($p = 0.0875$) (**Figure S4F**).

After ~5 months post fusion, MGEOs fully merged with COs and the entire assembloid became a single spherical structure (**Figure 6I**). mDLX-GFP+ interneurons within assembloids co-expressed GABA(**Figure S5A**) and exhibited robust process outgrowth with both bipolar and multipolar interneuron morphologies (**Figure S5B-C**). Immunostaining of assembloids at 9 months revealed robust expression of PV and Kv3.1, especially in the MGEO periphery (**Figure S5D-F**), and the formation of inhibitory synapses, with vGAT+ puncta closely apposed to Gephyrin+ puncta, onto the somas of putative cortical excitatory neurons marked by CAG-tdTomato (**Figure 6J**). vGAT+ puncta were also identified along Ankyrin G immunolabeled axon initial segments (**Figure 6K**), indicative of inhibitory axo-axonic synapses. These data suggest that MGEO-derived interneurons synaptically integrate with excitatory neurons in the COs.

MGEO-CO assembloids display functional integration of interneurons, complex activity and fast-spiking neurons

To provide evidence for functional synapses and examine neuronal activity, we next performed whole-cell patch-clamp and multielectrode array (MEA) recordings from MGEO-CO assembloids. Action potential (AP) firing and spontaneous post-synaptic currents in both excitatory and inhibitory neurons were examined using whole-cell recordings of slices made from 6-month-old assembloids (**Figure 7A-D**). We observed spontaneous AP firing in 50% (9 of 18 cells) of recorded neurons, and an additional 17% (3 of 18 cells) displayed repetitive AP firing upon depolarizing current injection (**Figure 7B, B'**, respectively). We also found that glutamatergic and GABAergic neurons formed functional connections, with recordings of mDLX-GFP-labeled interneurons displaying spontaneous excitatory post-synaptic currents (sEPSCs; **Figure 7C**) and CAG-tdTomato-labeled, putative excitatory neurons receiving spontaneous inhibitory post-synaptic currents (sIPSCs; **Figure 7D**). sIPSCs were also recorded after co-application of the AMPA and NMDA receptor antagonists CNQX and AVP to isolate GABAergic synapses(**Figure 7D'**).

Most published MEA recordings from brain organoids are conducted with the organoids chronically cultured on the MEA plates, leading to the migration of many neurons out of

the organoids onto the surface of the MEA plate[90]. This approach disrupts the 3D neural organoid cytoarchitecture and records activity from both 2D and 3D networks that may not faithfully replicate activity exclusively derived from 3D brain structures. To overcome this limitation, we transiently plated MGEO-CO assembloids grown in suspension onto MEA plates for recordings (**Figure 7E**), before placing them back in suspension culture, allowing for recordings made exclusively from 3D networks as well as subsequent recordings from the same organoid at later timepoints (see **Methods**). Inspection of the raw voltage time series revealed large-amplitude voltage fluctuations, the presence of both single- and multi-unit action potentials, and bursts of action potentials (recordings made at 212 and 235 DIV) (**Figure 7F**). We hypothesized that MGEO-CO assembloids would contain a significant number of MGE-derived high-firing-rate inhibitory neurons, as compared to CO-CO assembloids without interneurons. Consistent with this prediction, 140 DIV CO-CO assembloids exhibited a larger fraction of putative units with low firing rates relative to MGEO-CO assembloids (**Figure 7G**). This finding suggests that some of the MGE-derived interneurons in the MGEO-CO assembloids include fast-spiking interneurons, aligning with the observed increase in high-firing-rate units in MGEO-CO assembloids.

Raster plots of MGEO-CO assembloids recorded at DIV 140, 212, and 235 illustrate the expected emergence of network complexity and synchronicity as a function of organoid maturation (**Figure 7H**). Cumulative distribution analyses of maximum firing rates across different maturation stages revealed that firing rates at DIV 140 are significantly lower compared to those at DIV 212 and 235, while no significant difference was observed between DIV 212 and 235 (**Figure 7I**). Similarly, the cumulative distribution of the number of bursts increased over time, as DIV 140 assembloids exhibited significantly fewer bursts compared to DIV 212 and 235 **(Figure 7J**). No significant difference in number of bursts was observed for MGEO-CO assembloids between DIV 212 and 235 **(Figure 7J**); however, increased complexity of bursting patterns was observed in MGEO-CO assembloids at DIV 235 (**Figure S6**). Collectively, these data suggest that as MGEO-CO assembloids mature, both firing rates and network bursting activity increase and shift to complex bursting patterns between DIV 212 and 235.

To further confirm the presence of functional inhibitory neurons in MGEO-CO assembloids, we applied 10 µM bicuculline, a GABA-A receptor antagonist, to assess the role of GABAergic transmission in regulating network activity. Electrode-matched representative voltage traces from a 5-minute recording before and after bicuculline application showed clear alterations in firing rates with bicuculline exposure (**Figure 7K**). Quantification of this effect (**Figure 7L**) confirms that blocking GABAergic transmission leads to a net increase in firing rates within network bursts. In addition, we classified putative units from extracellular recordings to distinguish between fast-spiking (FS) and regular-spiking (RS) neurons using spike sorting and measurements of trough to peak (TTP) AP duration (**Figure 7M, N**).The majority of putative units in MGEO-CO assembloids were FS units, further supporting the presence of MGE-derived fast-spiking interneurons. These results provide direct evidence that inhibitory neurons in MGEO-CO assembloids are functionally integrated and that FS units are effectively generated in MGEO-CO assembloids.

Discussion

Here we describe a novel method for differentiating hPSCs into MGE-specified subpallial organoids. This MGEO model provides a valuable human-specific platform for future studies of the formation and maturation of cortical interneurons and other MGE-derived cell-types during human development and in neuropsychiatric disorders. Impairments in cortical interneurons derived from the MGE have been associated with various neurodevelopmental disorders, highlighting the broad potential applications of our model. Currently established human subpallial (ventral forebrain-patterned) organoid models generate GABAergic neurons that migrate into cortical organoids upon their fusion; however, these models show limited expression of MGE lineage cortical interneuron markers (e.g. LHX6) and are severely limited in the production of late-generated PV interneurons. Our self-organizing single rosette MGE organoids (MGEOs) overcome these limitations, exhibiting strong expression of MGE lineage markers (LHX6, NKX2.1, PV, and SST) and producing MGE-derived cortical- and subpallial-destined GABAergic neurons, astrocytes and rare oligodendrocytes.

This approach worked for MGEOs derived from hESC and blood- and fibroblast-derived iPSC lines. Notably, our SOSR protocol begins with a hPSC monolayer that is patterned towards neuroepithelium with dual-SMAD inhibition. Patterning initially as a monolayer allows for even distribution of morphogens across all cells which increases culture purity and better mimics the formation of the neural plate in human embryonic development. In contrast, other ventral telencephalic organoid models begin with hPSC aggregation into embryoid bodies which ultimately produce multi-rosette structures leading to irregularities in morphogen gradients across all cells. Therefore, the initial monolayer step of our MGEO model is likely advantageous for generating MGE-specific lineages, and the optimal timing of patterning factor application may differ for multi-rosette protocols.

Characterization of MGEOs using scRNA-seq, RT-qPCR, and immunostaining methods confirmed their highly reproducible MGE specificity and close alignment to human MGE fetal tissue transcriptomic profiles. Indeed, this work, to our knowledge, is the first to closely compare organoid transcriptomic profiles with human fetal MGE down to a sub-cluster level, and to demonstrate three human MGE lineages arising from an organoid protocol, including the presence of the human-specific CRABP1+ PV precursor. This study is also the first to show the robust generation of PV cortical interneurons in an organoid model, with PV expression appearing as early as 3 months *in vitro* and stabilizing to approximately 30-40% of the organoid area from 4 months onwards. PV cortical interneurons play a critical role in cortical information processing, regulating excitability and gamma oscillations,[92] and their dysfunction is implicated in various neuropsychiatric disorders; however, the late generation and prolonged maturation time of PV interneurons has historically limited the field's ability to derive and study them using hPSC models. Other hPSC-derived ventral brain organoid models generate minimal numbers of PV cortical interneurons. Recent studies show hPSC-derived human MGE-like pallial interneurons sorted and transplanted into mouse brains generate limited PV expression, even at 8-months post-transplantation, further underscoring the difficulty of deriving PV interneurons from hPSCs.[46] The ability of our

MGEO model to generate large numbers of PV+ cortical interneurons from 4 months *in vitro,* therefore, marks a significant advancement in the field, offering a unique platform to study the development of PV cortical interneurons and their associated disorders.

We assessed migration of GABAergic cells from MGEOs in both 2D assays and 3D MGEO-CO assembloids. In both assays, rapid and robust migration of mDLX-GFP+ cells was observed within hours, and the cells displayed properties indicative of migrating cortical interneurons/progenitors, including leading-edge branching and somal translocation. While previous studies have similarly demonstrated that interneurons from ventral patterned cortical organoids migrate and integrate with excitatory neurons in ventral:dorsal assembloids, migration in these models is relatively slow, with most migration timepoints shown as 1 month post-fusion. Furthermore, migration and fusion appear incomplete in these assembloid, with a large proportion of the ventral organoid often remaining distinctly separate from the cortical organoid. In contrast, our MGEO-CO assembloids fully fuse together to form a single sphere after prolonged culture. Given that the MGE is a transitory structure that gives rise to highly migratory cell-types, our MGEO protocol may more accurately model the development and integration of MGE-derived cells *in vivo.* The rapid and robust migration of MGE-derived neurons in MGEO-CO assembloids may perhaps be attributed to both MGEOs and COs containing a single main rosette structure, promoting the development and organization of ventricular and subventricular-like zones*,* as these regions have been shown to release guidance cues that repulse cortical interneurons[93–95]. Overall, the robust and reproducible migration of mDLX-GFP+ interneurons observed in our model supports the usefulness of MGEOs for investigating human MGE-derived cortical interneuron migration mechanisms and potential defects associated with brain disorders.

In terms of neuronal function, the patch-clamp recordings of MGEO-CO assembloid slices indicated MGEO-derived interneurons exhibit physiologically relevant functional maturation and integrate with cortical neurons in the assembloids. We also developed a novel technique to achieve MEA recordings from MGEO-CO assembloids, with minimal perturbations to them and allowing their continuous development after the recordings.

This method has the powerful advantage of allowing organoids to maintain their 3D structure and not reorganize their cytoarchitecture to become 2D structures, as often occurs when organoids are adhered to a flat surface for prolonged periods[96]. Our method is also cost and resource efficient as the same MEA plate can be used to record numerous batches of organoids consecutively across multiple timepoints. These same organoids can then be used for histological, molecular, or biochemical assays, increasing the amount and type of data that can be collected from each individual organoid and offering a unique opportunity to link organoid network activity with cell-type composition, interactions, or 3D cytoarchitecture.

Using this novel MEA recording approach, we identified waveforms that exhibited FS characteristics. We attribute this finding, which has not been described with other subpallial organoid protocols, to the ability of MGEOs to generate PV cortical interneurons, and to the novel electrophysiological approach which allows for established 3D network to remain intact and continue to mature. Additionally, the MGEO-derived GABAergic interneurons are enriched at the periphery of the assembloids (**Figure 3E**), in close juxtaposition to the extracellular electrodes where they would potentially contribute to a disproportionate identification of PV/FS-like cells. Moreover, we identified perineuronal nets and robust expression of $K_v3.1$, key features of PV FS interneurons, in assembloids at later timepoints. Our MEA recordings were performed at a sampling rate of 12.5 kHz, limiting the temporal resolution needed to accurately classify fast spike waveform features (e.g. trough to peak) faithfully. To increase the specificity of cell-type identification in future experiments, incorporating a reporter line that specifically labels PV cortical interneurons would enable selective targeting of these cells. For example, using an opto-tagging approach in combination with MEA recordings would allow for definitive identification and functional manipulation of PV FS cells based on waveform shape. Regardless of these limitations, our findings demonstrate MGEO-CO assembloid network maturation, including increased firing rates, burst dynamics, and the presence of functionally integrated MGEO-derived inhibitory neurons.

Overall, our novel hPSC-derived MGE-specific brain organoid model provides a valuable tool to study MGE-derived cortical interneuron development and for future modeling of interneuron-related phenotypes in genetic epilepsies and related neurodevelopmental disorders (see **Supplemental Figure S7** for expression of genes in MGEOs that are commonly implicated in neurodevelopmental disorders). Given the high LHX6+ MGE specificity of the MGEO model, the robust production of PV+ interneurons, and the presence of other key MGE-derived cell types, MGEOs may also serve as a potential source of MGE interneuron progenitors for therapeutic grafting to potentially treat epilepsies, ASD or neurodegenerative disorders associated with impairments in MGE-derived cortical interneurons.

Limitations of this study

Although results were predominantly consistent across all experimental replicates, we observed some variability between cell lines and samples, predominantly in scRNA-seq and RT-qPCR studies. Our electrophysiology experiments also showed some cell-line variations, particularly in their maturation timelines, with the fibroblast-derived line (2E) displaying slightly delayed electrophysiological development compared to the embryonic (H9) and blood-derived (79B) hPSC lines. These findings were supported by comparative analyses of the scRNA-seq data from 3-month MGEOs developed from all the hPSC lines and those from human fetal tissues at different gestational weeks (**Figure 5H**). These differences highlighted the importance of validating hPSC lines and the need to utilize proper isogenic or cell-line-origin matched controls when modeling diseases. Additionally, while the maturation time of MGEOs is considerably accelerated compared to *in vivo* human developmental timelines, we found that a prolonged maturation time of MGEOs *in vitro* was necessary for them to robustly express PV (~120 days) and to display complex network activity (~200 days). Further optimization of the MGEO protocol will be needed to further shorten this maturation period. Lastly, MGEOs must be individually removed from the thick extracellular matrix manually at 10-12 DIV, limiting large scalability of this method. Additional protocol optimizations are

therefore needed to identify an efficient way to overcome this rate-limiting protocol step.

Resource availability

Lead contact

Further information and requests for resources and reagents should be directed to the lead contact, Jack Parent (parent@med.umich.edu).

Materials availability

Materials used in this study are available upon request to the lead contact.

Data and code availability

- The data generated during this study are available from the lead contact upon request. Raw single cell RNAseq data will be deposited to GEO upon publication.
- The code used for scRNAseq analysis and spike sorting analysis will be available upon request.
- Any additional information required to reanalyze the data reported in this paper is available from the lead contact upon request.

Acknowledgments

Research reported in this publication was supported by the University of Michigan Advanced Genomics Core, the UM Single Cell Spatial Analysis Program and the National Cancer Institute under Award Number P30CA046592 by the use of the

following Cancer Center Shared Resource: Single Cell and Spatial Analysis Shared Resource. We would like to thank the University of Michigan Viral Vector Core for generating the viral reagents. We also gratefully acknowledge Paul Jenkins for the generous gift of the AnkG antibody. We also thank Maria Faraj for assisting with the AMD3100 migration experiments. This work was also supported by the National Institutes of Health (NIH; NS117170-JMP, NS129850-JF, NS076752-LLI), the National Science Foundation (NSF; EFMA 2422149-JF), the Simons Foundation Autism Research Initiative (JMP), the NSF Graduate Research Fellowship (DGE-2241144-MCV), the NIH Diversity Specialized Predoctoral to Postdoctoral Advancement in Neuroscience (D-SPAN) F99/K00 transition award (1F99NS135817-MCV), University of Michigan Rackham Merit Fellowship (MCV), T32 University of Michigan Training Program in Translational Research NIH-NIGMS Pre-doctoral Fellowship (5T32GM141840-02, 1T32GM141840-01-MPW), and the NIH Early Stage Training in the Neurosciences Training Grant (5T32NS076401-20-MPW). Some illustrations were created using BioRender.

Author contributions

Conceptualization: M.C.V., M.P.W., J.M.P. ; Methodology: M.C.V., M.P.W., J.M.P.; Data generation and analysis: M.C.V., M.P.W., T.T., L.G.; scRNA-seq data processing and analysis: J.B., M.C.V., M.P.W., J.Z.L., A.M.T.; Electrophysiology acquisition and analysis: Y.Y., M.C.V., E.L.C.; Writing of original draft: M.C.V, M.P.W with contributions from E.L.C., Y.Y., J.B.; Editing of original draft: J.M.P., M.U., A.M.T.; Review of final draft: all authors; Contribution of resources: J.M.P., M.U., L.L.I, A.M.T

Declaration of interests

The authors have no financial or other competing interests to declare.

STAR Methods

Key resources table

REAGENT or RESOURCE	SOURCE	IDENTIFIER
Antibodies		
Mouse Monoclonal Anti-**LHX6** Antibody	Santa Cruz Biotechnology	Cat# sc-271433; RRID: AB_10649856
Rabbit Polyclonal Anti- **Calretinin** Antibody	Millipore	Cat# AB5054; RRID: AB_2068506
Rat Monoclonal Anti-**Somatostatin** Antibody	Millipore	Cat# MAB354; RRID: AB_2255365
Mouse Monoclonal Anti-**Somatostatin** Antibody	Santa Cruz Biotechnology	Cat# sc-55565; RRID: AB_831726
Rabbit Polyclonal anti-**Glial Fibrillary Acidic Protein** (GFAP) Antibody	Agilent	Cat# Z0334; RRID: AB_10013382
Rabbit Polyclonal anti-**OLIG2** Antibody	Millipore	Cat# AB9610; RRID: AB_570666
Rat Monoclonal anti-**Myelin Basic Protein** (MBP), aa 82-87 Antibody	Millipore	Cat# MAB386; RRID: AB_94975
Rabbit Polyclonal Anti-**Parvalbumin** Antibody	Swant	Cat# PV27; RRID: AB_2631173
Rabbit Polyclonal anti-**K_v3.1b** (KCNC1) Antibody	Alamone	Cat# APC-014; RRID: AB_2040166
Mouse Monoclonal Anti-**MEF2C** Antibody	Novus Biologicals	Cat# NBP2-00493; RRID: AB_3245039
Wisteria floribunda lectin (**WFA**, WFL), Biotinylated	Vector Laboratories	Cat# B-1355; RRID: AB_2336874
Goat anti-**Ankyrin G** Antibody	Gift from Paul Jenkins Lab	N/A
Rabbit Polyclonal Anti-**vGAT** Antibody	Synaptic Systems	Cat# 131 003; RRID: AB_887869
Mouse Monoclonal Anti-**Map2ab** Antibody	Sigma-Aldrich	Cat# M4403; RRID: AB_477193
Mouse Monoclonal Anti-**Gephyrin** Antibody	Synaptic Systems	Cat# 147 011; RRID: AB_887717
Anti-Mouse Polyclonal Anti-**Pax6** Antibody	MBL International	Cat# PD022; RRID: AB_1520876
Mouse Monoclonal Anti-**SHH** Antibody	Santa Cruz Biotechnology	Cat# sc-365112; RRID: AB_10709580
Guinea Pig Polyclonal Anti-**Rx** Antibody	Takara	Cat# M229; RRID: AB_2783559
Mouse Monoclonal Anti-**NKX2.1** Antibody	Millipore	Cat# MAB5460; RRID: AB_571072
Goat anti-Mouse IgG (H+L) Highly Cross-Adsorbed Secondary Antibody, Alexa Fluor 488	Thermo Fisher Scientific	Cat# A-11029; RRID: AB_2534088

Goat anti-Mouse IgG (H+L) Cross-Adsorbed Secondary Antibody, Alexa Fluor 568	Thermo Fisher Scientific	Cat# A-11004; RRID: AB_2534072
Goat anti-Mouse IgG (H+L) Highly Cross-Adsorbed Secondary Antibody, Alexa Fluor 647	Thermo Fisher Scientific	Cat# A-21236; RRID: AB_2535805
Goat anti-Mouse IgG (H+L) Cross-Adsorbed Secondary Antibody, Alexa Fluor 405	Thermo Fisher Scientific	Cat# A-31553; RRID: AB_221604
Goat anti-Rabbit IgG (H+L) Cross-Adsorbed Secondary Antibody, Alexa Fluor 488	Thermo Fisher Scientific	Cat# A-11008; RRID: AB_143165
Goat anti-Rabbit IgG (H+L) Cross-Adsorbed Secondary Antibody, Alexa Fluor 568	Thermo Fisher Scientific	Cat# A-11011; RRID: AB_143157
Goat anti-Rabbit IgG (H+L) Highly Cross-Adsorbed Secondary Antibody, Alexa Fluor 647	Thermo Fisher Scientific	Cat# A-21245; RRID: AB_2535813
Goat anti-Rabbit IgG (H+L) Cross-Adsorbed Secondary Antibody, Alexa Fluor 405	Thermo Fisher Scientific	Cat# A-31556; RRID: AB_221605
Goat anti-Guinea Pig IgG (H+L) Highly Cross-Adsorbed Secondary Antibody, Alexa Fluor 647	Thermo Fisher Scientific	Cat# A-21450; RRID: AB_2535867
Donkey anti-Goat IgG (H+L) Cross-Adsorbed Secondary Antibody, Alexa Fluor 488	Thermo Fisher Scientific	Cat# A-11055; RRID: AB_2534102
Donkey anti-Rabbit IgG (H+L) Highly Cross-Adsorbed Secondary Antibody, Alexa Fluor 488	Thermo Fisher Scientific	Cat# A-21206; RRID: AB_2535792
Bacterial and virus strains		
pAAV_BiPVe3_dTomato_nls-dTomato	Furlanis et al.[97]	Addgene 213940
pAAV-mDLX-GFP_Fishell-1	Dimidschstein et al.[98]	Addgene 83900-AAV1
pAAV-CAG-tdTomato (codon diversified)	Edward Boyden	Addgene 59462-AAV1
Chemicals, peptides, and recombinant proteins		
DMEM/F12	Gibco	Cat# 11330032
mTeSR1	STEMCELL Tech	Cat# 85850
mTeSR Plus	STEMCELL Tech	Cat# 100-0276
Geltrex	Thermo Fisher Scientific	Cat# A1413302
AccuGENE 0.5M EDTA Solution	Lonza	Cat# 51201
Rho-kinase inhibitor (Y-27632)	Tocris	Cat# 1254
StemPro™ Accutase™	Thermo Fisher Scientific	Cat# A1110501
Neurobasal	Gibco	Cat# 21103049
N-2 Supplement	Gibco	Cat# 17502048
B-27 Supplement	Gibco	Cat# 17504044
B-27 Supplement minus Vitamin A	Gibco	Cat# 12587010
DMH1	Tocris	Cat# 4126
XAV939	Cayman Chemical	Cat# 13596
SB-431542	Cayman Chemical	Cat# 13031

Cyclopamine	Cayman Chemical	Cat# 11321
L7 Passaging Solution	Lonza	Cat# FP-5013
CHIR99021	Cayman Chemical	Cat# 13122
SAG	Selleckchem	Cat# S7779
Human FGF-basic (FGF-2/bFGF) (aa 1-155) Recombinant Protein	Gibco	Cat# PHG0261
Human Albumin	Sigma	Cat# A7223-1G
Human Brain Derived Neurotrophic Factor (BDNF)	Peprotech	Cat# 450-02-1MG
Human Neurotrophic factor-3 (NT3)	Peprotech	Cat# 450-03-50UG
MEM Non-Essential Amino Acids (MEM NEAA)	Gibco	Cat# 1140-050
Penicillin Streptomycin	Gibco	Cat# 14140-122
Glutamax (100X)	Gibco	Cat# 35050-061
BrainPhys Neuronal Medium with SM1 Kit	STEMCELL Tech	Cat# 5792
L-Ascorbic acid	Sigma	Cat# A92902-500G
Human GDNF	Peprotech	Cat# 450-10-1MG
HEPES (1M) Buffer Solution	Giibco	Cat# 15630-080
AMD3100	Tocris	Cat# 3299
Streptavidin, Alexa Fluor™ 647 Conjugate	Themo Fisher Scientific	Cat# S21374
Critical commercial assays		
RNeasy mini kit	Qiagen	Cat# 74104
RNase-Free DNase Set	Qiagen	Cat# 79254
SuperScript™ III First-Strand Synthesis SuperMix kit	Invitrogen	Cat# 11752-050
Power SYBR Green PCR Master Mix	Themo Fisher Scientific	Cat# 4367659
Chromium Next GEM Single Cell Fixed RNA Sample Preparation Kit	10x Genomics	Cat# 1000414
Deposited data		
Raw MGEO scRNAseq data	This paper	Available upon publication
Human reference genome NCBI build 38, patch 13 (GRCh38.p13)	Genome Reference Consortium	http://www.ncbi.nlm.nih.gov/projects/genome/assembly/grc/human/
scRNAseq from human ganglionic eminences at GW09, GW11, GW12, GW13, GW16, & GW18	Shi et al.[29]	GEO: GSE135827
scRNA-seq for hMGEO organoids derived from hPSCs	Xiang et al.[99]	GEO: GSE97882
scRNA-seq for hSS organoids derived from human iPSCs	Birey et al.[100]	GEO: GSE93811 and GSE96045
Experimental models: Cell lines		

Con2E (2E) Male Fibroblast-derived iPSC line	Tidball, et al.[101,102]	N/A
79B Female PBMC-derived iPSC line	Mojica-Perez, et al.[103]	N/A
H9 Female Embryonic hESC line	Thomas et al.[104]	WiCell cat# WA09 RRID:CVCL_9773
Oligonucleotides		
See Table S1 for RT-qPCR primer sequences		
Software and algorithms		
BioRender	N/A	RRID:SCR_018361
Fiji	Schindelin et al[105]	RRID:SCR_002285
RStudio (v4.4.1)	Posit team	RRID:SCR_000432
Seurat (v4.2.3)	Hao*, Hao*, et al.[106]	RRID:SCR_000432
Cell Ranger Single-Cell software suite (v7.1.0)	10x Genomics	RRID:SCR_017344
Loupe Browser	10x Genomics	RRID:SCR_018555
GraphPad Prism 10	N/A	RRID:SCR_002798
BCL Convert Conversion Software (bcl2fastq) v4.0	Illumina	RRID:SCR_015058
Other		
StemPro EZ passage tool	Thermo Fisher Scientific	Cat# 23181010
STRIPPER® Micropipetter	Cooper Surgical	Cat# MXL3-STR
275µM tips for STRIPPER Micropipetter	Cooper Surgical	Cat# MXL3-275
O.C.T.	Fisher Healthcare	Cat# 4585
Tissue-Tek Cryomolds	Sakura	Cat# 32663
Costar Ultra-low attachment 96-well round bottom plates	Corning	Cat# CLS7007-24EA
Costar 24-well Ultra-Low attachment plates	Corning	Cat# 3473

Supplementary Table S1: RT-qPCR Primers

Gene	Forward Primer	Reverse Primer	Source
RAX	AGCGAAACTGTCAGAGGAGGAACA	TCATGCAGCTGGTACGTGGTGAAA	Meyer et al.[107]
SHH	AAGATCTCCAGAAACTCCGAGCGA	CGAGATGGCCAAAGCGTTCAACTT	Cao et al.[108]
KCNC1 (Kv3.1)	GCGCTCCTCTGGACAACA	TTGGTCATCTCCAGCTCGTC	This paper

NKX2.1	GCAGACAGACTGACAGACACG	CAGTCGCCAACAAATGAGC	Li et al.[109]
LHX6	AGCTGCTACATCAAGAACAAGG	AGTCGCTGGCGTAGATCTGT	This paper
PAX6	CAGCTTCACCATGGCAAATA	GCAGCATGCAGGAGTATGAG	This paper
FOXG1	AACCTGTGTTGCGCAAATGC	AAACACGGGCATATGACCAC	Birey et al.[100]
vGAT	CACGACAAGCCCAAAATCAC	CAGGATGGCGTAGGGTAGG	This paper
SST	GCTGCTGTCTGAACCCAAC	CGTTCTCGGGGTGCCATAG	Birey et al[100]
KCC2 (SLC12A5)	GCCACCATGCTAAACAACCT	TCTGTGTCGGTGCTGTTGAT	This paper
NKCC1	ATCCCACTGGAGAGCAAGAA	TTCCTTTGGGTATGGCTGAC	This paper
MEF2C	TCACTGTTGTGCTCCTTTGC	ATGAGTGCCATACGCCAATG	Fujii et al.[110]
LHX8	GGACCAGCTTTACAGCAGATCAG	CGTCTGCTCAAGCCTGTCCTTT	This paper
GAPDH	AAGGTGAAGGTCGGAGTCAA	AATGAAGGGGTCATTGATGG	This paper
Mycoplasma	TGCACCATCTGTCATTCTGTT	GGGAGCAAACAGGATTAGATA	Mojica-Perez et al.[111]

Human Pluripotent Stem Cell Culture

All hPSC experiments were conducted with prior approval from the University of Michigan Human Pluripotent Stem Cell Research Oversight (HPSCRO) Committee. To ensure the reproducibility of our MGEO protocol, experiments were replicated using three hPSC lines, one hESC line and two iPSC lines one each derived from fibroblasts and peripheral blood mononuclear cells, and including both male and female lines. Cultures were maintained in incubators dedicated to hPSCs, which were kept at 37°C with humidity control and 5% CO2. Prior to organoid differentiation, stem cells were maintained in mTeSR-1 (STEMCELL Technologies, Cat# 85850) or mTeSR-Plus (STEMCELL Technologies, Cat # 100-0276) feeder-free medium on 6-well tissue culture plates coated with 1:100 Geltrex (Thermo Fisher scientific A1413302). Cells were regularly passaged when they reached approximately 60-70% confluency using 0.8mM EDTA. Cell lines were routinely tested for mycoplasma and monitored for morphology and spontaneous differentiation. The genomic integrity and pluripotency of these cell lines was confirmed by Single Nucleotide Polymorphism (SNP) chip DNA Microarray and immunostaining for pluripotency markers, respectively[58,59,111,112].

MGEO generation

Self-organizing single rosette MGEOs were generated from a hPSC monolayer by modifying our SOSR-CO protocol (Tidball et al., 2023b). For the initial formation of the monolayer, iPSC lines were dissociated using Accutase (Innovative cell) and plated onto Geltrex-coated (1:50 dilution in DMEM/F12) 12-well plates at 3–4 × 10^5 cells/mL in mTeSR1 with 10 µM Rho-kinase inhibitor (Y-27632; Tocris, 1254). Media without the inhibitor was replaced daily until the cells reached 80%–100% confluency. The medium was then changed to 3N (50:50 DMEM/F12:Neurobasal with N2 and B27 supplements) without vitamin A with 2 µM DMH1 (Tocris, 4126), 2 µM XAV939 (Cayman Chemical, 13596), and 10 µM SB431542 (Cayman Chemical, 13031) (2 mL of media per well). On DIV 4, media was removed, and the monolayer was incubated for 1 min with L7 hPSC passaging solution (Lonza). After aspirating the L7 solution, the monolayer was cut into squares using a StemPro EZ passage tool. The squares were sprayed off the bottom of the culture plate with 1 mL of pre-prepared culture media with a P1000 micropipette. Approximately 200 µL of resuspended squares were then transferred into each well of a 96-well plate preincubated at 37°C for 30 min with 40 µL of 100% Geltrex solution/well. Each monolayer will seed up to 16 wells containing approximately 20-40 organoids per well. Additional media was added to each well the day after plating without media change. Half-media changes were performed daily beginning 48 hrs post plating. On day 6 (2 days after cutting), human FGF2 (20 ng/ml, Gibco, PHG0261) was added to the culture media to support cell survival. On day 10, a 100% media change was performed with 3N media plus 100 nM SAG (Selleckchem, S7779) and FGF2, without DMH1, XAV939 and SB431542. Between days 10 and 12, the organoids were individually removed using a STRIPPER Micropipetter (Cooper Surgical) with 275 µm tips and placed in suspension individually in the wells of a low-adherence U-bottom 96-well plate with 200 µL of 3N medium without vitamin A. The ideal diameter for picking the MGEOs is ∼250 µM. Larger sizes may produce additional rosettes, and smaller sizes tend to have suboptimal survival. Starting on day 12, half-media changes (100 µL/well) of 3N with vitamin A, 100 nM SAG, BDNF (20 ng/mL), and NT3 (20 ng/mL) without FGF2 were repeated every other day until day 18 when SAG was removed from

the culture medium. After 35 days of differentiation, 3N media with vitamin A (but without BDNF and NT3) was used for half-media changes every other day. At this time, MGEOs were transferred to low-adherence 24-well plates for a necessary increase in media volume due to expanded organoid size. Beginning day 90, MGEOs were cultured in BrainPhys media (Stemcell technologies, 05790) containing N2 supplement, NeuroCult™ SM1 Neuronal Supplement (Stemcell technologies, 05711), BDNF (20 ng/mL), GDNF (20 ng/mL), and Ascorbic acid (200nM). Self-organizing single rosette cortical organoids (SOSR-COs) were generated as described[58].

Cryopreservation, sectioning and immunocytochemistry

Organoids were collected, washed with phosphate-buffered saline (PBS), and incubated in 4% paraformaldehyde (PFA) diluted in PBS at 4°C for 30 min (for 1 month organoids) or an hour (for older organoids). After three 10-min PBS washes, organoids were incubated overnight at 4°C in a 30% sucrose (in PBS) solution, embedded in cryomolds (Tissue-Tek 4566) using O.C.T compound (Fisher Healthcare 4585), frozen on dry ice, and stored at -80°C. Frozen organoid blocks were sectioned onto Superfrost Plus glass slides (ThermoFisher 12-550-15) at a thickness of 20µM using a Leica CM1850 cryostat. After drying at room temperature (RT) for at least 2 h, slides were stored at -20°C until use. For immunostaining, organoid sections were washed three times with PBS, permeabilized for 20 min in PBS with 0.2% Triton-X100 at RT, and incubated in blocking buffer (PBS with 0.05% Tween- 20, 5% normal goat serum, and 1% bovine serum albumin (BSA)) for 1 h at RT. Normal horse serum was used in blocking buffer for immunostaining using goat primary antibodies. Fixed and permeabilized sections were incubated overnight at 4°C in a humidified chamber with primary antibodies diluted in blocking buffer. Sections were then washed 3 times in PBST (PBS with 0.05% Tween-20) and incubated for 2 hours at RT with Alexa-Flour secondary antibodies diluted 1:500 in blocking buffer. Sections were washed once with PBST for 10 minutes and incubated with bisbenzimide for 5 min to label nuclei. After 3x-10 min washes of PBST, coverslips were mounted onto slides using Glycergel mounting medium (Agilent Dako C0563). Once set, the edges of the slides were sealed using clear nail polish. Slides containing immunolabeled organoid sections were imaged using an Andor BC43

benchtop spinning disc confocal microscope (Oxford Instruments). Acquired images were analyzed in Fiji.

RT-qPCR

For reverse transcriptase quantitative PCR (RT-qPCR), total RNA was extracted using the miRNeasy Mini Kit (Qiagen 217004) as per manufacturer's protocols (with optional DNase1 digestion step), with at least four organoids pooled per sample. Template RNA (100 ng) was used to synthesize cDNA using the SuperScript™ III First-Strand Synthesis SuperMix kit (Invitrogen 11752-050). RT-qPCR was performed as per manufacturer protocols, using 2 ng of cDNA and Power SYBR Green PCR Master Mix (Thermofisher 4367659) with an AppliedBiosystems QuantStudio3 thermocycler (see **Supplemental Table S1** for primer sequences). Fold changes were calculated using the $2^{-\Delta\Delta Ct}$ method, normalizing to the average undifferentiated 2E iPSC levels from n=3-4 experiments. Samples were run in triplicate and GAPDH was used as an internal control. Undetectable levels of mRNA were set to a CT value of 40 for analysis, which was performed in Microsoft Excel and graphed using GraphPad Prism.[58]

Fixation of whole MGE organoids

For samples generated using our initial ventralizing protocol (**Figure S1**), scRNA-seq data collection and downstream analysis was performed as previously described[58]. For the MGEO protocol, whole organoid fixation for downstream scRNA-seq analysis of MGEOs was conducted using the 10X Genomics Chromium Next GEM Single Cell Fixed RNA Sample Preparation Kit (10X Genomics, 1000414). All reagents described below were supplied with the kit and the protocol was carried out as described on the 10X Genomics website. In brief, 4-8 organoids (depending on age/size) were collected using a P1000 micropipette with a cut pipette tip and transferred to a 1.5 mL Eppendorf tube. Organoids were allowed to sink to the bottom of the tube and the supernatant media was carefully aspirated from the tube without disturbing the organoids. Organoids were rinsed once with 1 ml of PBS, the PBS was removed from the tube and 500 ml of Fixation Buffer was added and incubated for 24 h. at 4°C. The next day, the Fixation Buffer was removed without disturbing the organoids and the organoids were washed

with 1 mL of chilled PBS. PBS was removed and 500 µL of Quenching Buffer was added to the tube containing the fixed organoids. Enhancer (50 µL) was added and pipette mixed. Glycerol (137.5 µL of a 50% solution) was then added and pipette mixed for a final concertation of 10% glycerol. Samples were stored in -80°C until they were sent to the University of Michigan's Advanced Genomics core for further processing and analysis.

MGEO tissue dissociation, library prep, and sequencing

Tissue dissociation, library prep and next-generation sequencing was carried out in the Advanced Genomics Core at the University of Michigan. Fixed organoid tissue samples were dissociated, then individual samples were barcoded, and pooled together for sequencing. Cells were processed through the 10x Genomics Chromium system (10x Genomics). 10x Genomics v.3 libraries were prepared according to the manufacturer's instructions. Libraries were then sequenced using paired-end sequencing with a mean coverage ranging from 15,000 to 39,000 raw reads per cell using an Illumina NovaSeqXPlus. Day 90 pooled samples were subjected to 28x90bp of sequencing according to the manufacturer's protocol (Illumina NovaSeqXPlus). scRNA-seq data were aligned and quantified using Cell Ranger Single-Cell software suite (v.7.1.0, 10x Genomics) against Homo sapiens (human) genome assembly GRCh38.p13 from ENSEMBL. BCL Convert Conversion Software v4.0 (Illumina) was used to generate de-multiplexed Fastq files.

Analysis of scRNAseq data

Analysis of scRNA-seq data was done as previously reported[113]. Briefly, the data were analyzed using the R package Seurat (v.4.2.3, https://satijalab.org/seurat/)). Datasets were filtered, normalized, and scaled. Differences between G2/M phase and S phase scores were regressed out during the scaling process. The dataset further went through PCA analysis and was embedded into low-dimensional space using UMAP algorithm for visualization. Clusters were identified using shared nearest neighbor modularity optimization-based clustering algorithm. The clusters were annotated based on

expression of known marker genes and genes found to identify specific cell types in human fetal MGE data sets [29,33,45].

To compare our day 90 MGEO scRNA-seq data to human fetal GE expression, we used the Shi *et al.* dataset [29], which includes scRNA-seq data from MGE, LGE, and CGE human fetal tissue at GW 9, 12, 16, and 18. A PCA plot was used to determine how closely related the gene expression profile of our MGEO samples were to the GW9-19 human dataset's regional and cell type clusters, and to determine the GW age to which the MGEOs were most similar. A Pearson correlation was used to compare day 90 MGEO neuronal clusters 1-7 to human fetal MGE subclusters. To assess regional specificity and determine the extent to which MGEOs more closely recapitulate MGE-like expression markers, we compared the percentage of cells expressing key regional and interneuron gene markers between our MGEO scRNA-seq dataset, established subpallial organoid protocols[49,50], and the Shi *et al*. human MGE cluster.

The number and percentage of cells expressing key regional and interneuron gene markers in each dataset was calculated and plotted using a custom R function. In brief, gene expression percentages were calculated across different Seurat objects, combined into a data frame, transformed using the melt() function, and visualized for comparison across datasets using ggplot2. To visualize the number of neurons expressing one or more interneuron subtype-specific markers, neuronal clusters (clusters 1-7) were extracted from the day 90 MGEO data set and the top five subtype specific gene markers (based on the percentage of neurons expressing each marker) were selected for multi gene expression analysis. All valid gene combinations were identified using a custom R function and the number of neurons with single or multi gene expression profiles was plotted using ggplot2.

Viral labeling and generation of cortical-MGEO assembloids

To visualize migrating neurons in assembloids, cortical organoids (SOSR-COs) were labeled with codon diversified AAV1-CAG-tdTomato (Addgene # 59462), while interneuron progenitors and interneurons were labeled in MGEOs using AAV1-mDlx-GFP (Addgene # 83900) virus prior to fusion, as previously described[114]. Briefly, 46 DIV

organoids were transferred into 1.5 mL Eppendorf tubes and incubated overnight (37°C, 5% CO2) in 250 µL of 3N with vitamin A organoid culture media containing diluted virus (1:50). Fresh 3N media with Vitamin A (750 µL) was added the next day. The following day, organoids were washed with PBS to remove residual virus, then transferred to ultra-low attachment plates with fresh culture media for maintenance until fusion into assembloids approximately one week later. To generate MGEO-cortical assembloids, SOSR-CO and MGEO regions with the brightest viral reporter expression were placed in contact with each other along the bottom edge of a 48- or 24-well plate. Plates were tilted at an angle to ensure the organoids maintained contact with each other, and left undisturbed for at least 24 hours. At later stages, PV basket cells were labeled in assembloids with AAV1-BiPVe3-dTomato_nls-dTomato (Addgene # 213940) virus using the same methods as above.

2D assay of MGEO neuronal migration

To interrogate the migration of interneurons from 3D MGEOs onto 2D extra-cellular matrix, 21 DIV organoids were plated into individual wells of a 1:50 Geltrex-coated, thin-bottom, black-walled 96-well culture plate (PerkinElmer 6055300) containing 3N+A media. Organoids were gently moved to the center of each well using a pipette tip and allowed to settle to the bottom of the well. Automated live imaging of migration in phase or brightfield was performed using an Incucyte S3 Live Cell Analysis System or Andor BC43 benchtop spinning disc confocal microscope. Using the Incucyte, multiple 10x images were acquired per well at 15-min intervals over 48 h, starting immediately after plating. Andor confocal microscope images were collected at 5-10 min intervals over 15 h, beginning at least 2 h post plating. For both imaging methods, cultures were maintained at 37°C and 5% CO2. Plates were fixed with 4% PFA at 48 h post-plating for immunostaining, which was performed as described above.

To block CXCR4, a receptor that regulates the migration of interneurons in the developing neocortex[87,88], the CXCR4 antagonist AMD3100 (100 nM) was added to organoid media[49]. For the “chronic” exposure condition, AMD3100 was added beginning 6 days prior to the migration assay (24 DIV), with a half media change containing fresh

100 nM drug performed every 2-3 d. For the “acute” groups, 100 nM of drug was added at the time of plating for the migration assay (30 DIV). Incucyte images were taken as described above and Fiji ImageJ was used to quantify the area of cell migration (onto ECM) between control, acute, and chronic conditions at 48-h post plating. The organoid area and spots of debris were excluded prior to quantification. Experiments were performed using 8 MGEOs per condition from 2 differentiations derived from the 79B hPSC line. Graphpad Prism was used to graph the migrated neuron area of each replicate organoid and for statistical analysis (see below).

Live imaging of assembloids, 3D migration, and quantification

To assess interneuron migration in a 3D environment, SOSR-COs and MGEOs were virally labeled and fused at 56 DIV as described above. Live imaging of GFP+, migrating cells was conducted using the Andor BC43 benchtop spinning disk confocal microscope. Migration in assembloids was imaged every 5 min for 15 h. Static confocal images of live assembloids were also collected at multiple timepoints between 24 h to 15 d post fusion to assess migration over time. mDLX-GFP labeled cells that migrated into the cortical organoid area were quantified in Fiji as the percent of GFP area in the CAG-TdTom area and plotted using Graphpad Prism.

Complementing our 2D neuronal migration experiments above, we exposed 79B-derived assembloids to the CXCR4 antagonist AMD3100 (or no drug control) 1 day post MGEO-CO fusion. We imaged and quantified the area of mDLX-GFP MGEO interneurons that migrated into CO organoid 24 h later, as described above.

Multi-electrode array (MEA) recordings

Assembloids (at 20-34 wk differentiation) were plated individually in each well of a 6-well cytoview MEA plate (Axion Biosystems, Atlanta, GA, USA) coated with ploy-L-ornithine (PLO) (100 µg/mL) and Geltrex (1:100). As opposed to the conventional method of organoid MEA recording, wherein organoids grow chronically on the MEA plate, which alters their 3D cytoarchitecture over time, we transferred each organoid to

the MEA plate immediately before recording and carefully removed the majority of the media after positioning the organoid on top of the electrodes. This method takes advantage of the adhesion properties of liquid, allowing the organoid to firmly contact the electrodes as the media is removed. After a 5-min recording, media was added back into the MEA plate and the organoid was gently removed from the MEA plate and maintained in suspension culture. The reproducibility of MEA recordings was verified by removing, replating, and then re-recording from the same organoid several times over a short time window and across multiple MEA wells to ensure consistency of signal (data not shown).

All recordings were performed using a Maestro MEA system and AxIS Software in Spontaneous Neural Configuration (Axion Biosystems). MEA signals were sampled at 12.5 kHz and bandpass filtered at 200-3000 Hz with Butterworth filtering to detect APs. APs were detected using a threshold of 5.5 times the standard deviation of the noise. Single electrode bursts were detected as a minimum of five APs occurring with a maximum interval of 100 ms. Network bursts were detected as a minimum of 50 APs with 100 ms maximum inter-AP interval observed on a minimum of 25% of active electrodes. Mean firing rate estimation was determined within a 10 s window and synchrony parameters were detected using a window size of 20 ms.

Patch-clamp recording of organoid slices

Procedures for cutting organoid slices were similar to those used for acute mouse brain slices. The slicing solution contained (in mM): 110 sucrose; 62.5 NaCl; 2.5 KCl; 7.5 $MgCl_2$; 1.25 $KH2PO_4$; 26 $NaHCO_3$; 0.5 $CaCl_2$ and 20 D-glucose (pH 7.35-7.4 when saturated with 95% O2 /5% CO2 at room temperature of 22-25° C). To prepare fresh organoid slices, one assembloid (1-2 mm) was manually cut into 4-6 slices (~300 µm) in ice-cold, oxygenated “slicing” solution saturated with 95% O_2 /5% CO_2. Slices were incubated in slicing solution for 15-20 min at RT and then in a mixture (1:1) of slicing solution and artificial cerebrospinal fluid (ACSF), the latter containing (in mM): 125 NaCl; 2.5 KCl; 1 $MgCl_2$; 1.25 $KH2PO_4$; 26 $NaHCO_3$; 2 $CaCl_2$ and 20 D-glucose, (pH

7.35-7.4), in a holding chamber aerated continuously with 95% O_2 /5% CO_2 at 35° C for 30 min before transfer to ACSF at RT.

Procedures for electrophysiological recordings in assembloid slices were similar to those used previously for acute mouse brain slices or for cultured iPSC-derived neurons[112,115–117]. An assembloid slice was transferred to a recording chamber where it was perfused (2-3 ml/min) with ACSF bubbled continuously with 95% O_2 /5% CO_2. The mDLX-GFP-labeled interneurons and CAG-tdTom labeled pyramidal cells were visually selected using a NIKON E600FN upright microscope equipped with Nomarski optics (x 40 water immersion objective). For recording of AP firing, recording electrodes had resistances of 4-7 MΩ when filled with a potassium gluconate (K-gluconate)-based pipette solution consisting of (in mM): 140, K-gluconate; 4, NaCl; 0.5, $CaCl_2$; 10, HEPES; 5, EGTA, 5 phophocreatine; 2, Mg-ATP and 0.4, GTP (pH 7.2-7.3 adjusted with KOH). Repetitive firing and AP frequencies from individual neurons were examined using the whole cell current-clamp recording technique. Repetitive AP firing was evoked by injection of a series of 1500 ms depolarizing currents varying from -60 pA to 200 pA at 10 pA-step from resting membrane potentials. Spontaneous AP firing was recorded in the gap-free model from resting membrane potentials. The pipette solution for spontaneous inhibitory synaptic current (sIPSC) recordings consisted of (in mM): 140, CsCl; 4, NaCl; 0.5, CaCl2; 10, HEPES; 5, EGTA, 5 phosphocreatine; 2, Mg-ATP and 0.4, GTP (pH 7.3 adjusted with CsOH). Signals were amplified with a Multiclamp 700B amplifier (Molecular Devices, Sunnyvale, CA), filtered at 2-4 kHz and digitized at 20 kHz for off-line analysis. Data were acquired with a Digidata 1440A interface and analyzed using pClamp11 offline. All experiments were carried out at RT (22-25°C).

Statistics

GraphPad Prism 10.2.2 was used for all statistical analyses. In Figures 1 and 3, RT-qPCR data are presented as mean ± SEM, with each dot representing a single experimental replicate sample, which is composed of data from 4-8 pooled organoids. Migration data is graphed as mean ± SD with each dot being a datapoint from a single organoid. One-way ANOVA with Tukey multiple comparisons correction analysis was

used to determine the statistical significance in migrated neuron area between control, acute, and chronic AMD3100 treatments 48 h post plating for 2D migration assays. Student T-test statistical comparison was used to compare the effects of control vs AMD3100 treatment on the area of mDLX-GFP MGEO interneuron migration into the CO organoid area of MGEO-CO fusion 48 h post-fusion. Experimental conditions were blinded during analysis. In all graphs, dot shapes denote the hPSC lines from which organoids were derived (circle for 79B, triangle for 2E, diamond for H9). For comparisons of MEA firing patterns (Figure 7), cumulative distribution of maximum firing rates and burst counts were compared via two-tailed Kolmogorov-Smirnov test. Firing rate per burst before and after bicuculline exposure was compared using two-tailed Mann-Whitney test.

References

1. Buzsáki, G., and Chrobak, J.J. (1995). Temporal structure in spatially organized neuronal ensembles: a role for interneuronal networks. Curr Opin Neurobiol *5*, 504–510. https://doi.org/10.1016/0959-4388(95)80012-3.

2. Hájos, N., Pálhalini, J., Mann, E.O., Nèmeth, B., Paulsen, O., and Freund, T.F. (2004). Spike Timing of Distinct Types of GABAergic Interneuron during Hippocampal Gamma Oscillations In Vitro. The Journal of Neuroscience *24*, 9127. https://doi.org/10.1523/JNEUROSCI.2113-04.2004.

3. Jacobs, J., Kahana, M.J., Ekstrom, A.D., and Fried, I. (2007). Brain oscillations control timing of single-neuron activity in humans. Journal of Neuroscience *27*, 3839–3844. https://doi.org/10.1523/JNEUROSCI.4636-06.2007,.

4. Bartos, M., Vida, I., Frotscher, M., Meyer, A., Monyer, H., Geiger, J.R.P., Jonas, P., and Heidelberg (2002). Fast synaptic inhibition promotes synchronized gamma oscillations in hippocampal interneuron networks. Proc Natl Acad Sci U S A *99*, 13222–13227. https://doi.org/10.1073/PNAS.192233099,.

5. Marín, O. (2012). Interneuron dysfunction in psychiatric disorders. Nat Rev Neurosci *13*, 107–120. https://doi.org/10.1038/nrn3155.

6. Vogt, D., Cho, K.K.A., Shelton, S.M., Paul, A., Huang, Z.J., Sohal, V.S., and Rubenstein, J.L.R. (2018). Mouse Cntnap2 and Human CNTNAP2 ASD Alleles Cell Autonomously Regulate PV + Cortical Interneurons. Cerebral Cortex *28*, 3868–3879. https://doi.org/10.1093/CERCOR/BHX248.

7. Chen, Q., Deister, C.A., Gao, X., Guo, B., Lynn-Jones, T., Chen, N., Wells, M.F., Liu, R., Goard, M.J., Dimidschstein, J., et al. (2020). Dysfunction of cortical GABAergic neurons leads to sensory hyper-reactivity in a Shank3 mouse model of ASD. Nat Neurosci *23*, 520–532. https://doi.org/10.1038/S41593-020-0598-6.

8. Smith, A.L., Jung, E.M., Jeon, B.T., and Kim, W.Y. (2020). Arid1b haploinsufficiency in parvalbumin- or somatostatin-expressing interneurons leads to distinct ASD-like and ID-like behavior. Sci Rep *10*. https://doi.org/10.1038/S41598-020-64066-5.

9. Amegandjin, C.A., Choudhury, M., Jadhav, V., Carriço, J.N., Quintal, A., Berryer, M., Snapyan, M., Chattopadhyaya, B., Saghatelyan, A., and Di Cristo, G. (2021). Sensitive period for rescuing parvalbumin interneurons connectivity and social behavior deficits caused by TSC1 loss. Nat Commun *12*. https://doi.org/10.1038/S41467-021-23939-7.

10. Nomura, T. (2021). Interneuron dysfunction and inhibitory deficits in autism and fragile X syndrome. Cells *10*. https://doi.org/10.3390/CELLS10102610.

11. Juarez, P., and Martínez Cerdeño, V. (2022). Parvalbumin and parvalbumin chandelier interneurons in autism and other psychiatric disorders. Front Psychiatry *13*. https://doi.org/10.3389/FPSYT.2022.913550/FULL.

12. Lupien-Meilleur, A., Jiang, X., Lachance, M., Taschereau-Dumouchel, V., Gagnon, L., Vanasse, C., Lacaille, J.C., and Rossignol, E. (2021). Reversing frontal disinhibition rescues behavioural deficits in models of CACNA1A-associated neurodevelopment disorders. Mol Psychiatry *26*, 7225–7246. https://doi.org/10.1038/S41380-021-01175-1.

13. Ferguson, B., Glick, C., and Huguenard, J.R. (2023). Prefrontal PV interneurons facilitate attention and are linked to attentional dysfunction in a mouse model of absence epilepsy. Elife *12*. https://doi.org/10.7554/ELIFE.78349.

14. Rossignol, E., Kruglikov, I., Van Den Maagdenberg, A.M.J.M., Rudy, B., and Fishell, G. (2013). CaV2.1 ablation in cortical interneurons selectively impairs fast-spiking basket cells and causes generalized seizures. Ann Neurol *74*, 209–222. https://doi.org/10.1002/ANA.23913.

15. Jiang, X., Lachance, M., and Rossignol, E. (2016). Involvement of cortical fast-spiking parvalbumin-positive basket cells in epilepsy. Prog Brain Res *226*, 81–126. https://doi.org/10.1016/BS.PBR.2016.04.012.

16. Jiang, X., Lupien-Meilleur, A., Tazerart, S., Lachance, M., Samarova, E., Araya, R., Lacaille, J.C., and Rossignol, E. (2018). Remodeled cortical inhibition prevents

motor seizures in generalized epilepsy. Ann Neurol *84*, 436–451. https://doi.org/10.1002/ANA.25301.

17. Gertler, T.S., Cherian, S., DeKeyser, J.M., Kearney, J.A., and George, A.L. (2022). KNa1.1 gain-of-function preferentially dampens excitability of murine parvalbumin-positive interneurons. Neurobiol Dis *168*. https://doi.org/10.1016/J.NBD.2022.105713.

18. Ryner, R.F., Derera, I.D., Armbruster, M., Kansara, A., Sommer, M.E., Pirone, A., Noubary, F., Jacob, M., and Dulla, C.G. (2023). Cortical Parvalbumin-positive interneuron development and function are altered in the APC conditional knockout mouse model of infantile and epileptic spasms. Soc NeuroscienceRF Ryner, ID Derera, M Armbruster, A Kansara, ME Sommer, A Pirone, F Noubary, M JacobJournal of Neuroscience, 2023•Soc Neuroscience *43*, 1422–1440. https://doi.org/10.1523/JNEUROSCI.0572-22.2022.

19. Sohal, V.S., and Rubenstein, J.L.R. (2019). Excitation-inhibition balance as a framework for investigating mechanisms in neuropsychiatric disorders. Mol Psychiatry *24*, 1248–1257. https://doi.org/10.1038/S41380-019-0426-0.

20. Shen, M., Guo, Y., Dong, Q., Gao, Y., Stockton, M.E., Li, M., Kannan, S., Korabelnikov, T., Schoeller, K.A., Sirois, C.L., et al. (2021). FXR1 regulation of parvalbumin interneurons in the prefrontal cortex is critical for schizophrenia-like behaviors. Mol Psychiatry *26*, 6845–6867. https://doi.org/10.1038/S41380-021-01096-Z.

21. Lewis, D.A. (2014). Inhibitory neurons in human cortical circuits: substrate for cognitive dysfunction in schizophrenia. Curr Opin Neurobiol *26*, 22–26. https://doi.org/10.1016/J.CONB.2013.11.003.

22. Gabitto, M.I., Travaglini, K.J., Rachleff, V.M., Kaplan, E.S., Long, B., Ariza, J., Ding, Y., Mahoney, J.T., Dee, N., Goldy, J., et al. (2024). Integrated multimodal cell atlas of Alzheimer's disease. Nature Neuroscience 2024 27:12 *27*, 2366–2383. https://doi.org/10.1038/s41593-024-01774-5.

23. Xu, Q., Cobos, I., De, E., Cruz, L., Rubenstein, J.L., and Anderson, S.A. (2004). Origins of cortical interneuron subtypes. Soc NeuroscienceQ Xu, I Cobos, E De La Cruz, JL Rubenstein, SA AndersonJournal of Neuroscience, 2004•Soc Neuroscience. https://doi.org/10.1523/JNEUROSCI.5667-03.2004.

24. Xu, Q., Tam, M., and Anderson, S.A. (2008). Fate mapping Nkx2.1-lineage cells in the mouse telencephalon. Journal of Comparative Neurology *506*, 16–29. https://doi.org/10.1002/CNE.21529.

25. Flames, N., Pla, R., Gelman, D.M., Rubenstein, J.L.R., Puelles, L., and Marín, O. (2007). Delineation of multiple subpallial progenitor domains by the combinatorial expression of transcriptional codes. Soc NeuroscienceN Flames, R Pla, DM Gelman, JLR Rubenstein, L Puelles, O MarínJournal of Neuroscience, 2007•Soc Neuroscience. https://doi.org/10.1523/JNEUROSCI.2750-07.2007.

26. Anderson, S.A., Marín, O., Horn, C., Jennings, K., and Rubenstein, J.L.R. (2001). Distinct cortical migrations from the medial and lateral ganglionic eminences. Development *128*, 353–363. https://doi.org/10.1242/DEV.128.3.353.

27. Anderson, S.A., Kaznowski, C.E., Horn, C., Rubenstein, J.L.R., and McConnell, S.K. (2002). Distinct origins of neocortical projection neurons and interneurons in vivo. Cereb Cortex *12*, 702–709. https://doi.org/10.1093/CERCOR/12.7.702.

28. Wonders, C.P., and Anderson, S.A. (2006). The origin and specification of cortical interneurons. Nature Reviews Neuroscience 2006 7:9 *7*, 687–696. https://doi.org/10.1038/nrn1954.

29. Shi, Y., Wang, M., Mi, D., Lu, T., Wang, B., Dong, H., Zhong, S., Chen, Y., Sun, L., Zhou, X., et al. (2021). Mouse and human share conserved transcriptional programs for interneuron development. Science (1979) *374*. https://doi.org/10.1126/SCIENCE.ABJ6641.

30. Nicholas, C.R., Chen, J., Tang, Y., Southwell, D.G., Chalmers, N., Vogt, D., Arnold, C.M., Chen, Y.J.J., Stanley, E.G., Elefanty, A.G., et al. (2013). Functional maturation of hPSC-derived forebrain interneurons requires an extended timeline and mimics human neural development. Cell Stem Cell *12*, 573–586. https://doi.org/10.1016/j.stem.2013.04.005.

31. Maroof, A.M., Keros, S., Tyson, J.A., Ying, S.W., Ganat, Y.M., Merkle, F.T., Liu, B., Goulburn, A., Stanley, E.G., Elefanty, A.G., et al. (2013). Directed differentiation and functional maturation of cortical interneurons from human embryonic stem cells. Cell Stem Cell *12*, 559–572. https://doi.org/10.1016/j.stem.2013.04.008.

32. Keefe, F., Monzón-Sandoval, J., Rosser, A.E., Webber, C., and Li, M. (2023). Single-Cell Transcriptomics Reveals Conserved Regulatory Networks in Human and Mouse Interneuron Development. Int J Mol Sci *24*. https://doi.org/10.3390/IJMS24098122.

33. Zhao, Z., Zhang, D., Yang, F., Xu, M., Zhao, S., Pan, T., Liu, C., Liu, Y., Wu, Q., Tu, Q., et al. (2022). Evolutionarily conservative and non-conservative regulatory networks during primate interneuron development revealed by single-cell RNA and ATAC sequencing. Cell Research 2022 32:5 *32*, 425–436. https://doi.org/10.1038/s41422-022-00635-9.

34. Zhao, Y., Flandin, P., Long, J.E., Dela Cuesta, M., Westphal, H., and Rubenstein, J.L.R. (2008). Distinct molecular pathways of development of telencephalic interneuron subtypes revealed through analysis of Lhx6 mutants. Journal of Comparative Neurology *510*, 79–99. https://doi.org/10.1002/CNE.21772.

35. Fogarty, M., Grist, M., Gelman, D., Marín, O., Pachnis, V., and Kessaris, N. (2007). Spatial genetic patterning of the embryonic neuroepithelium generates GABAergic interneuron diversity in the adult cortex. Soc NeuroscienceM Fogarty, M Grist, D Gelman, O Marín, V Pachnis, N KessarisJournal of Neuroscience, 2007•Soc Neuroscience *27*, 10935–10946. https://doi.org/10.1523/JNEUROSCI.1629-07.2007.

36. Liodis, P., Denaxa, M., Grigoriou, M., Akufo-Addo, C., Yanagawa, Y., and Pachnis, V. (2007). Lhx6 activity is required for the normal migration and specification of cortical interneuron subtypes. Soc NeuroscienceP Liodis, M Denaxa, M Grigoriou, C Akufo-Addo, Y Yanagawa, V PachnisJournal of Neuroscience, 2007•Soc Neuroscience *27*, 3078–3089. https://doi.org/10.1523/JNEUROSCI.3055-06.2007.

37. Lim, L., Mi, D., Llorca, A., and Marín, O. (2018). Development and Functional Diversification of Cortical Interneurons. Neuron *100*, 294–313. https://doi.org/10.1016/J.NEURON.2018.10.009.

38. Sussel, L., Marin, O., Kimura, S., and Rubenstein, J.L.R. (1999). Loss of Nkx2.1 homeobox gene function results in a ventral to dorsal molecular respecification within the basal telencephalon: evidence for a transformation of the pallidum into the striatum. Development *126*, 3359–3370. https://doi.org/10.1242/DEV.126.15.3359.

39. Neves, G., Shah, M.M., Liodis, P., Achimastou, A., Denaxa, M., Roalfe, G., Sesay, A., Walker, M.C., and Pachnis, V. (2013). The LIM homeodomain protein Lhx6 regulates maturation of interneurons and network excitability in the mammalian cortex. Cereb Cortex *23*, 1811–1823. https://doi.org/10.1093/CERCOR/BHS159.

40. Vogt, D., Hunt, R.F., Mandal, S., Sandberg, M., Silberberg, S.N., Nagasawa, T., Yang, Z., Baraban, S.C., and Rubenstein, J.L.R. (2014). Lhx6 directly regulates Arx and CXCR7 to determine cortical interneuron fate and laminar position. Neuron *82*, 350–364. https://doi.org/10.1016/J.NEURON.2014.02.030.

41. Jakovcevski, I., Mayer, N., and Zecevic, N. (2010). Multiple Origins of Human Neocortical Interneurons Are Supported by Distinct Expression of Transcription Factors. Cerebral Cortex (New York, NY) *21*, 1771. https://doi.org/10.1093/CERCOR/BHQ245.

42. Zhao, Y., Marín, O., Hermesz, E., Powell, A., Flames, N., Palkovits, M., Rubenstein, J.L.R., and Westphal, H. (2003). The LIM-homeobox gene Lhx8 is required for the development of many cholinergic neurons in the mouse forebrain. Proc Natl Acad Sci U S A *100*, 9005–9010. https://doi.org/10.1073/PNAS.1537759100.

43. Wichterle, H., Garcia-Verdugo, J.M., Herrera, D.G., and Alvarez-Buylla, A. (1999). Young neurons from medial ganglionic eminence disperse in adult and embryonic brain. Nature Neuroscience 1999 2:5 *2*, 461–466. https://doi.org/10.1038/8131.

44. Alzu'bi, A., Lindsay, S., Kerwin, J., Looi, S.J., Khalil, F., and Clowry, G.J. (2017). Distinct cortical and sub-cortical neurogenic domains for GABAergic interneuron precursor transcription factors NKX2.1, OLIG2 and COUP-TFII in early fetal human telencephalon. Brain Struct Funct *222*, 2309–2328. https://doi.org/10.1007/S00429-016-1343-5.

45. Yu, Y., Zeng, Z., Xie, D., Chen, R., Sha, Y., Huang, S., Cai, W., Chen, W., Li, W., Ke, R., et al. (2021). Interneuron origin and molecular diversity in the human fetal brain. Nat Neurosci *24*, 1745–1756. https://doi.org/10.1038/S41593-021-00940-3.

46. Bershteyn, M., Bröer, S., Parekh, M., Maury, Y., Havlicek, S., Kriks, S., Fuentealba, L., Lee, S., Zhou, R., Subramanyam, G., et al. (2023). Human pallial MGE-type GABAergic interneuron cell therapy for chronic focal epilepsy. Cell Stem Cell *30*, 1331-1350.e11. https://doi.org/10.1016/J.STEM.2023.08.013.

47. Sloan, S.A., Andersen, J., Pa□ca, A.M., Birey, F., and Pa□ca, S.P. (2018). Generation and assembly of human brain region–specific three-dimensional cultures. Nature Protocols 2018 13:9 *13*, 2062–2085. https://doi.org/10.1038/s41596-018-0032-7.

48. Bagley, J.A., Reumann, D., Bian, S., Lévi-Strauss, J., and Knoblich, J.A. (2017). Fused cerebral organoids model interactions between brain regions. Nature Methods 2017 14:7 *14*, 743–751. https://doi.org/10.1038/nmeth.4304.

49. Birey, F., Andersen, J., Makinson, C.D., Islam, S., Wei, W., Huber, N., Fan, H.C., Metzler, K.R.C., Panagiotakos, G., Thom, N., et al. (2017). Assembly of functionally integrated human forebrain spheroids. Nature *545*, 54–59. https://doi.org/10.1038/nature22330.

50. Xiang, Y., Tanaka, Y., Patterson, B., Kang, Y.J., Govindaiah, G., Roselaar, N., Cakir, B., Kim, K.Y., Lombroso, A.P., Hwang, S.M., et al. (2017). Fusion of Regionally Specified hPSC-Derived Organoids Models Human Brain Development and Interneuron Migration. Cell Stem Cell *21*, 383-398.e7. https://doi.org/10.1016/j.stem.2017.07.007.

51. Sohal, V.S., Zhang, F., Yizhar, O., and Deisseroth, K. (2009). Parvalbumin neurons and gamma rhythms enhance cortical circuit performance. Nature *459*, 698–702. https://doi.org/10.1038/NATURE07991;KWRD=SCIENCE.

52. Gonzalez-Burgos, G., and Lewis, D.A. (2012). NMDA Receptor Hypofunction, Parvalbumin-Positive Neurons, and Cortical Gamma Oscillations in Schizophrenia. Schizophr Bull *38*, 950. https://doi.org/10.1093/SCHBUL/SBS010.

53. Avilés, E.C., Wilson, N.H., and Stoeckli, E.T. (2013). Sonic hedgehog and Wnt: Antagonists in morphogenesis but collaborators in axon guidance. Front Cell Neurosci. https://doi.org/10.3389/FNCEL.2013.00086/FULL.

54. Stoeckli, E.T. (2009). Morphogens and Neural Development. Encyclopedia of Neuroscience, 2397–2401. https://doi.org/10.1007/978-3-540-29678-2_3562.

55. Liem, J., Jessell, T.M., and Briscoe, J. (2000). Regulation of the neural patterning activity of sonic hedgehog by secreted BMP inhibitors expressed by notochord and somites. Development *127*, 4855–4866. https://doi.org/10.1242/DEV.127.22.4855.

56. Flandin, P., Zhao, Y., Vogt, D., Jeong, J., Long, J., Potter, G., Westphal, H., and Rubenstein, J.L.R. (2011). Lhx6 and Lhx8 Coordinately Induce Neuronal Expression of Shh that Controls the Generation of Interneuron Progenitors. Neuron *70*, 939. https://doi.org/10.1016/J.NEURON.2011.04.020.

57. Kohtz, J.D., Baker, D.P., Corte, G., and Fishell, G. (1998). Regionalization within the mammalian telencephalon is mediated by changes in responsiveness to Sonic Hedgehog. Development *125*, 5079–5089. https://doi.org/10.1242/DEV.125.24.5079.

58. Tidball, A.M., Niu, W., Ma, Q., Takla, T.N., Walker, J.C., Margolis, J.L., Mojica-Perez, S.P., Sudyk, R., Deng, L., Moore, S.J., et al. (2023). Deriving early single-rosette brain organoids from human pluripotent stem cells. Stem Cell Reports *18*, 2498–2514. https://doi.org/10.1016/J.STEMCR.2023.10.020.

59. Niu, W., Deng, L., Mojica-Perez, S.P., Tidball, A.M., Sudyk, R., Stokes, K., and Parent, J.M. (2024). Abnormal cell sorting and altered early neurogenesis in a human cortical organoid model of Protocadherin-19 clustering epilepsy. Front Cell Neurosci *18*. https://doi.org/10.3389/FNCEL.2024.1339345/FULL.

60. Takla, T.N., Luo, J., Sudyk, R., Huang, J., Walker, J.C., Vora, N.L., Sexton, J.Z., Parent, J.M., and Tidball, A.M. (2023). A Shared Pathogenic Mechanism for Valproic Acid and SHROOM3 Knockout in a Brain Organoid Model of Neural Tube Defects. Cells *12*. https://doi.org/10.3390/CELLS12131697,.

61. Birey, F., Andersen, J., Makinson, C.D., Islam, S., Wei, W., Huber, N., Fan, H.C., Metzler, K.R.C., Panagiotakos, G., Thom, N., et al. (2017). Assembly of functionally integrated human forebrain spheroids. Nature *545*, 54–59. https://doi.org/10.1038/NATURE22330;TECHMETA=100,13,14,38;SUBJMETA=2182,2571,378,532,631;KWRD=DEVELOPMENT+OF+THE+NERVOUS+SYSTEM,NEURAL+STEM+CELLS.

62. Xiang, Y., Tanaka, Y., Patterson, B., Kang, Y.J., Govindaiah, G., Roselaar, N., Cakir, B., Kim, K.Y., Lombroso, A.P., Hwang, S.M., et al. (2017). Fusion of Regionally Specified hPSC-Derived Organoids Models Human Brain Development and Interneuron Migration. Cell Stem Cell *21*, 383-398.e7. https://doi.org/10.1016/j.stem.2017.07.007.

63. Mo, Z., and Zecevic, N. (2008). Is Pax6 critical for neurogenesis in the human fetal brain? Cereb Cortex *18*, 1455–1465. https://doi.org/10.1093/CERCOR/BHM181.

64. Nóbrega-Pereira, S., Gelman, D., Bartolini, G., Pla, R., Pierani, A., and Marín, O. (2010). Origin and molecular specification of globus pallidus neurons. Soc NeuroscienceS Nóbrega-Pereira, D Gelman, G Bartolini, R Pla, A Pierani, O MarínJournal of Neuroscience, 2010•Soc Neuroscience *30*, 2824–2834. https://doi.org/10.1523/JNEUROSCI.4023-09.2010.

65. He, Z., Dony, L., Fleck, J.S., Szałata, A., Li, K.X., Slišković, I., Lin, H.-C., Santel, M., Atamian, A., Quadrato, G., et al. (2024). An integrated transcriptomic cell atlas of human neural organoids. Nature 2024 635:8039 *635*, 690–698. https://doi.org/10.1038/s41586-024-08172-8.

66. Du, T., Xu, Q., Ocbina, P.J., and Anderson, S.A. (2008). NKX2.1 specifies cortical interneuron fate by activating Lhx6. Development *135*, 1559–1567. https://doi.org/10.1242/DEV.015123.

67. Rakić, S., Kanatani, S., Hunt, D., Faux, C., Cariboni, A., Chiara, F., Khan, S., Wansbury, O., Howard, B., Nakajima, K., et al. (2015). Cdk5 phosphorylation of ErbB4 is required for tangential migration of cortical interneurons. Cerebral Cortex *25*, 991–1003. https://doi.org/10.1093/CERCOR/BHT290.

68. Fragkouli, A., van Wijk, N.V., Lopes, R., Kessaris, N., and Pachnis, V. (2009). LIM homeodomain transcription factor-dependent specification of bipotential MGE progenitors into cholinergic and GABAergic striatal interneurons. Development *136*, 3841–3851. https://doi.org/10.1242/DEV.038083.

69. Flandin, P., Kimura, S., Neuroscience, J.R.-J. of, and 2010, undefined (2010). The progenitor zone of the ventral medial ganglionic eminence requires Nkx2-1 to

generate most of the globus pallidus but few neocortical interneurons. Soc NeuroscienceP Flandin, S Kimura, JLR RubensteinJournal of Neuroscience, 2010•Soc Neuroscience *30*, 2812–2823. https://doi.org/10.1523/JNEUROSCI.4228-09.2010.

70. Kessaris, N., Fogarty, M., Iannarelli, P., Grist, M., Wegner, M., and Richardson, W.D. (2006). Competing waves of oligodendrocytes in the forebrain and postnatal elimination of an embryonic lineage. Nat Neurosci *9*, 173–179. https://doi.org/10.1038/NN1620.

71. Minocha, S., Valloton, D., Ypsilanti, A.R., Fiumelli, H., Allen, E.A., Yanagawa, Y., Marin, O., Chédotal, A., Hornung, J.P., and Lebrand, C. (2015). Nkx2.1-derived astrocytes and neurons together with Slit2 are indispensable for anterior commissure formation. Nat Commun *6*. https://doi.org/10.1038/NCOMMS7887.

72. Butt, S.J.B., Fuccillo, M., Nery, S., Noctor, S., Kriegstein, A., Corbin, J.G., and Fishell, G. (2005). The temporal and spatial origins of cortical interneurons predict their physiological subtype. Neuron *48*, 591–604. https://doi.org/10.1016/J.NEURON.2005.09.034.

73. Pai, E.L.L., Chen, J., Darbandi, S.F., Cho, F.S., Chen, J., Lindtner, S., Chu, J.S., Paz, J.T., Vogt, D., Paredes, M.F., et al. (2020). Maf and mafb control mouse pallial interneuron fate and maturation through neuropsychiatric disease gene regulation. Elife *9*. https://doi.org/10.7554/ELIFE.54903.

74. Allaway, K.C., Gabitto, M.I., Wapinski, O., Saldi, G., Wang, C.Y., Bandler, R.C., Wu, S.J., Bonneau, R., and Fishell, G. (2021). Genetic and epigenetic coordination of cortical interneuron development. Nature *597*, 693–697. https://doi.org/10.1038/S41586-021-03933-1.

75. Kaczmarek, L.K., and Zhang, Y. (2017). Kv3 Channels: Enablers of Rapid Firing, Neurotransmitter Release, and Neuronal Endurance. Physiol Rev *97*, 1431–1468. https://doi.org/10.1152/PHYSREV.00002.2017.

76. Härtig, W., Brauer, K., and Brückner, G. (1992). Wisteria floribunda agglutinin-labelled nets surround parvalbumin-containing neurons. Neuroreport *3*, 869–872. https://doi.org/10.1097/00001756-199210000-00012.

77. Favuzzi, E., Marques-Smith, A., Deogracias, R., Winterflood, C.M., Sánchez-Aguilera, A., Mantoan, L., Maeso, P., Fernandes, C., Ewers, H., and Rico, B. (2017). Activity-Dependent Gating of Parvalbumin Interneuron Function by the Perineuronal Net Protein Brevican. Neuron *95*, 639-655.e10. https://doi.org/10.1016/J.NEURON.2017.06.028.

78. Furlanis, E., Dai, M., Leyva Garcia, B., Tran, T., Vergara, J., Pereira, A., Gorissen, B.L., Wills, S., Vlachos, A., Hairston, A., et al. (2025). An enhancer-AAV toolbox to target and manipulate distinct interneuron subtypes. Neuron *113*, 1525-1547.e15. https://doi.org/10.1016/J.NEURON.2025.05.002.

79. Xiang, Y., Tanaka, Y., Patterson, B., cell, Y.K.-C. stem, and 2017, undefined Fusion of regionally specified hPSC-derived organoids models human brain development and interneuron migration. cell.comY Xiang, Y Tanaka, B Patterson, YJ Kang, G Govindaiah, N Roselaar, B Cakir, KY KimCell stem cell, 2017•cell.com.

80. Wu, S.J., Sevier, E., Dwivedi, D., Saldi, G.A., Hairston, A., Yu, S., Abbott, L., Choi, D.H., Sherer, M., Qiu, Y., et al. (2023). Cortical somatostatin interneuron subtypes form cell-type-specific circuits. Neuron *111*, 2675-2692.e9. https://doi.org/10.1016/J.NEURON.2023.05.032/ASSET/6CFA747C-FE1C-4984-9320-AED19E7E55C3/MAIN.ASSETS/GR6.JPG.

81. Munguba, H., Nikouei, K., Hochgerner, H., Oberst, P., Kouznetsova, A., Ryge, J., Muñoz-Manchado, A.B., Close, J., Batista-Brito, R., Linnarsson, S., et al. (2023). Transcriptional maintenance of cortical somatostatin interneuron subtype identity during migration. Neuron *111*, 3590-3603.e5. https://doi.org/10.1016/J.NEURON.2023.07.018.

82. Zhang, C., Xie, Z., and Wang, N. (2025). Single-cell RNA sequencing of adult primate neocortex reveals the regulatory dynamics of neural plasticity. Am J Transl Res *17*, 2562. https://doi.org/10.62347/ZEOR5569.

83. Valiente, M., migration, F.M.-C. adhesion &, and 2009, undefined (2009). Migration of cortical interneurons relies on branched leading process dynamics. Taylor & FrancisM Valiente, FJ MartiniCell adhesion & migration, 2009•Taylor & Francis *3*, 278–280. https://doi.org/10.4161/cam.3.3.8832.

84. Nadarajah, B., Alifragis, P., Wong, R.O.L., and Parnavelas, J.G. (2003). Neuronal migration in the developing cerebral cortex: Observations based on real-time imaging. Cerebral Cortex *13*, 607–611. https://doi.org/10.1093/CERCOR/13.6.607.

85. Pla, R., Borrell, V., Flames, N., Neuroscience, O.M.-J. of, and 2006, undefined (2006). Layer acquisition by cortical GABAergic interneurons is independent of Reelin signaling. Soc NeuroscienceR Pla, V Borrell, N Flames, O MarínJournal of Neuroscience, 2006•Soc Neuroscience. https://doi.org/10.1523/JNEUROSCI.0245-06.2006.

86. Toudji, I., Toumi, A., Chamberland, É., and Rossignol, E. (2023). Interneuron odyssey: molecular mechanisms of tangential migration. Front Neural Circuits *17*. https://doi.org/10.3389/FNCIR.2023.1256455/FULL.

87. Stumm, R.K., Zhou, C., Ara, T., Lazarini, F., Dubois-Dalcq, M., Nagasawa, T., Höllt, V., and Schulz, S. (2003). CXCR4 regulates interneuron migration in the developing neocortex. Journal of Neuroscience *23*, 5123–5130. https://doi.org/10.1523/JNEUROSCI.23-12-05123.2003.

88. Wang, Y., Li, G., Stanco, A., Long, J.E., Crawford, D., Potter, G.B., Pleasure, S.J., Behrens, T., and Rubenstein, J.L.R. (2011). CXCR4 and CXCR7 Have Distinct Functions in Regulating Interneuron Migration. Neuron *69*, 61–76. https://doi.org/10.1016/j.neuron.2010.12.005.

89. Dimidschstein, J., Chen, Q., Tremblay, R., Rogers, S.L., Saldi, G.A., Guo, L., Xu, Q., Liu, R., Lu, C., Chu, J., et al. (2016). A viral strategy for targeting and manipulating interneurons across vertebrate species. Nat Neurosci *19*, 1743–1749. https://doi.org/10.1038/NN.4430.

90. Trujillo, C.A., Gao, R., Negraes, P.D., Gu, J., Buchanan, J., Preissl, S., Wang, A., Wu, W., Haddad, G.G., Chaim, I.A., et al. (2019). Complex oscillatory waves emerging from cortical organoids model early human brain network development. Cell Stem Cell *25*, 558. https://doi.org/10.1016/J.STEM.2019.08.002.

91. Amin, N.D., Kelley, K.W., Kaganovsky, K., Onesto, M., Hao, J., Miura, Y., McQueen, J.P., Reis, N., Narazaki, G., Li, T., et al. (2024). Generating human neural diversity with a multiplexed morphogen screen in organoids. Cell Stem Cell *31*, 1831-1846.e9. https://doi.org/10.1016/J.STEM.2024.10.016.

92. Magloire, V., Mercier, M.S., Kullmann, D.M., and Pavlov, I. (2019). GABAergic Interneurons in Seizures: Investigating Causality With Optogenetics. Neuroscientist *25*, 344–358. https://doi.org/10.1177/1073858418805002.

93. Zhu, Y., Li, H.S., Zhou, L., Wu, J.Y., and Rao, Y. (1999). Cellular and molecular guidance of GABAergic neuronal migration from an extracortical origin to the neocortex. Neuron *23*, 473–485. https://doi.org/10.1016/S0896-6273(00)80801-6/ASSET/95CA742C-BFD1-498E-A115-532107523A67/MAIN.ASSETS/GR7.JPG.

94. Marín, O., Yaron, A., Bagri, A., Tessier-Lavigne, M., and Rubenstein, J.L.R. (2001). Sorting of striatal and cortical interneurons regulated by semaphorin-neuropilin interactions. Science *293*, 872–875. https://doi.org/10.1126/SCIENCE.1061891.

95. Zimmer, G., Garcez, P., Rudolph, J., Niehage, R., Weth, F., Lent, R., and Bolz, J. (2008). Ephrin-A5 acts as a repulsive cue for migrating cortical interneurons. Eur J Neurosci *28*, 62–73. https://doi.org/10.1111/J.1460-9568.2008.06320.X.

96. Trujillo, C.A., Gao, R., Negraes, P.D., Gu, J., Buchanan, J., Preissl, S., Wang, A., Wu, W., Haddad, G.G., Chaim, I.A., et al. (2019). Complex Oscillatory Waves Emerging from Cortical Organoids Model Early Human Brain Network Development. Cell Stem Cell *25*, 558-569.e7. https://doi.org/10.1016/j.stem.2019.08.002.

97. Furlanis, E., Dai, M., Leyva Garcia, B., Tran, T., Vergara, J., Pereira, A., Gorissen, B.L., Wills, S., Vlachos, A., Hairston, A., et al. (2025). An enhancer-AAV toolbox to target and manipulate distinct interneuron subtypes. Neuron *113*, 1525-1547.e15. https://doi.org/10.1016/j.neuron.2025.05.002.

98. Dimidschstein, J., Chen, Q., Tremblay, R., Rogers, S.L., Saldi, G.A., Guo, L., Xu, Q., Liu, R., Lu, C., Chu, J., et al. (2016). A viral strategy for targeting and manipulating interneurons across vertebrate species. Nat Neurosci *19*, 1743–1749. https://doi.org/10.1038/nn.4430.

99. Xiang, Y., Tanaka, Y., Patterson, B., Kang, Y.J., Govindaiah, G., Roselaar, N., Cakir, B., Kim, K.Y., Lombroso, A.P., Hwang, S.M., et al. (2017). Fusion of Regionally Specified hPSC-Derived Organoids Models Human Brain Development and Interneuron Migration. Cell Stem Cell *21*, 383-398.e7. https://doi.org/10.1016/j.stem.2017.07.007.

100. Birey, F., Andersen, J., Makinson, C.D., Islam, S., Wei, W., Huber, N., Fan, H.C., Metzler, K.R.C., Panagiotakos, G., Thom, N., et al. (2017). Assembly of functionally integrated human forebrain spheroids. Nature *545*, 54–59. https://doi.org/10.1038/nature22330.

101. Tidball, A.M., Dang, L.T., Glenn, T.W., Kilbane, E.G., Klarr, D.J., Margolis, J.L., Uhler, M.D., and Parent, J.M. (2017). Rapid Generation of Human Genetic Loss-of-Function iPSC Lines by Simultaneous Reprogramming and Gene Editing. Stem Cell Reports *9*. https://doi.org/10.1016/j.stemcr.2017.07.003.

102. Tidball, A.M., Niu, W., Ma, Q., Takla, T.N., Walker, J.C., Margolis, J.L., Mojica-Perez, S.P., Sudyk, R., Deng, L., Moore, S.J., et al. (2023). Deriving early single-rosette brain organoids from human pluripotent stem cells. Stem Cell Reports *18*, 2498–2514. https://doi.org/10.1016/j.stemcr.2023.10.020.

103. Mojica-Perez, S., Stokes, K., Jacobs, S., Huang, J., Vaid, S., Yuan, Y., Pearson, C.A., Montes, D., Tidball, A., VanHeyningen, D., et al. (2025). Cryopreservation of

Human Cortical Organoids Using Vitrification. Biorxiv Preprint. https://doi.org/10.1101/2025.04.08.647634.

104. Thomson, J.A. (1998). Embryonic stem cell lines derived from human blastocysts. Science (1979) *282*. https://doi.org/10.1126/science.282.5391.1145.

105. Schindelin, J., Arganda-Carreras, I., Frise, E., Kaynig, V., Longair, M., Pietzsch, T., Preibisch, S., Rueden, C., Saalfeld, S., Schmid, B., et al. (2012). Fiji: An open-source platform for biological-image analysis. Preprint, https://doi.org/10.1038/nmeth.2019 https://doi.org/10.1038/nmeth.2019.

106. Hao, Y., Hao, S., Andersen-Nissen, E., Mauck, W.M., Zheng, S., Butler, A., Lee, M.J., Wilk, A.J., Darby, C., Zager, M., et al. (2021). Integrated analysis of multimodal single-cell data. Cell *184*, 3573-3587.e29. https://doi.org/10.1016/j.cell.2021.04.048.

107. Meyer, J.S., Shearer, R.L., Capowski, E.E., Wright, L.S., Wallace, K.A., Mcmillan, E.L., Zhang, S.-C., and Gamm, D.M. (2009). Modeling early retinal development with human embryonic and induced pluripotent stem cells. Proc. Natl. Acad. Sci. *106*, 16698–16703.

108. Cao, S.Y., Hu, Y., Chen, C., Yuan, F., Xu, M., Li, Q., Fang, K.H., Chen, Y., and Liu, Y. (2017). Enhanced derivation of human pluripotent stem cell-derived cortical glutamatergic neurons by a small molecule. Sci Rep *7*. https://doi.org/10.1038/s41598-017-03519-w.

109. Li, Y., Eggermont, K., Vanslembrouck, V., and Verfaillie, C.M. (2013). NKX2-1 activation by SMAD2 signaling after definitive endoderm differentiation in human embryonic stem cell. Stem Cells Dev *22*, 1433–1442. https://doi.org/10.1089/scd.2012.0620.

110. Fujii, T., Murata, K., Mun, S.H., Bae, S., Lee, Y.J., Pannellini, T., Kang, K., Oliver, D., Park-Min, K.H., and Ivashkiv, L.B. (2021). MEF2C regulates osteoclastogenesis and pathologic bone resorption via c-FOS. Bone Res *9*. https://doi.org/10.1038/s41413-020-00120-2.

111. Mojica-Perez, S., Stokes, K., Jacobs, S., Huang, J., Vaid, S., Yuan, Y., Pearson, C.A., Montes, D., Tidball, A., VanHeyningen, D., et al. (2025). Cryopreservation of Human Cortical Organoids Using Vitrification. bioRxiv, 2025.04.08.647634. https://doi.org/10.1101/2025.04.08.647634.

112. Tidball, A.M., Lopez-Santiago, L.F., Yuan, Y., Glenn, T.W., Margolis, J.L., Clayton Walker, J., Kilbane, E.G., Miller, C.A., Martina Bebin, E., Scott Perry, M., et al. (2020). Variant-specific changes in persistent or resurgent sodium current in

SCN8A-related epilepsy patient-derived neurons. Brain *143*, 3025–3040. https://doi.org/10.1093/BRAIN/AWAA247.

113. Xue, X., Kim, Y.S., Ponce-Arias, A.I., O'Laughlin, R., Yan, R.Z., Kobayashi, N., Tshuva, R.Y., Tsai, Y.H., Sun, S., Zheng, Y., et al. (2024). A patterned human neural tube model using microfluidic gradients. Nature *628*, 391–399. https://doi.org/10.1038/S41586-024-07204-7.

114. Sloan, S., Andersen, J., Pa□ca, A., protocols, F.B.-N., and 2018, undefined Generation and assembly of human brain region–specific three-dimensional cultures. nature.comSA Sloan, J Andersen, AM Pa□ca, F Birey, SP Pa□caNature protocols, 2018•nature.com.

115. Yuan, Y., O'Malley, H.A., Smaldino, M.A., Bouza, A.A., Hull, J.M., and Isom, L.L. (2019). Delayed maturation of GABAergic signaling in the Scn1a and Scn1b mouse models of Dravet Syndrome. Sci Rep *9*. https://doi.org/10.1038/S41598-019-42191-0.

116. Yuan, Y., Lopez-Santiago, L., Denomme, N., Chen, C., O'Malley, H.A., Hodges, S.L., Ji, S., Han, Z., Christiansen, A., and Isom, L.L. (2024). Antisense oligonucleotides restore excitability, GABA signalling and sodium current density in a Dravet syndrome model. Brain *147*, 1231–1246. https://doi.org/10.1093/BRAIN/AWAD349.

117. Lopez-Santiago, L.F., Yuan, Y., Wagnon, J.L., Hull, J.M., Frasier, C.R., O'Malley, H.A., Meisler, M.H., and Isom, L.L. (2017). Neuronal hyperexcitability in a mouse model of SCN8A epileptic encephalopathy. Proc Natl Acad Sci U S A *114*, 2383–2388. https://doi.org/10.1073/PNAS.1616821114.

Figure Legends

Figure 1: Generation of human subpallial brain organoids with MGE regional specificity

(A) Schematic of tangential migration of MGE-derived interneurons, key markers differentiating MGE from nearby brain regions, and the distribution of key patterning molecules Sonic Hedgehog (SHH) and Wingless-related Integration Site (WNT).

(B) Protocol variations tested for generating brain organoids with MGE regional specificity. DXSB condition: 2uM DMH1, 2uM XAV939, 10uM SB431542.

(C) Heat map of relative mRNA levels measured by qRT-PCR in 18 DIV organoids exposed to various timings and concentrations of SAG and with or without continued (cont.) XAV939 after DXSB. n=1-2 differentiations per condition of 2E iPSCs. Graphed as Log_{10}FC relative to GAPDH and iPSC baseline. Text in blue indicates the condition that most closely produced the expected MGE regional expression levels (high *LHX6*, low *PAX6* and *RX*).

(D) Final protocol for generating MGEOs. Boxes in blue above the timeline illustrate the key steps at days 4 (monolayer cutting) and 10 (transitioning organoids from 3D adherent to suspension culture).

(E) Relative mRNA expression of 1-, 2- and 3-month MGEOs for key regional markers. n≥5 differentiations between 3 cell lines. Graphed as average ΔΔCT fold change ± SEM, normalized to GAPDH and relative to average iPSC baseline. Shapes denote hPSC line and colors indicate age (triangle: 2E, circle: 79B, diamond: H9; gray: 1 month, purple: 2 month, orange: 3 month).

(F) immunostaining of MGEOs at 1-month (top) and 3-months (bottom) shows the expected strong expression of GABA (green), LHX6 (red), NKX2-1 (green), and Olig2 (red). Bisbenzimide nuclear stain (DNA) is in blue. A higher magnification view is shown in the inset of each image.

Abbreviations: NCx: Neocortex; LGE: Lateral Ganglionic Eminence; Str: Striatum; GP: Globus pallidus; MGE: medial ganglionic eminence; POA: preoptic area; Hyp: Hypothalamus; ECM: extracellular matrix.

Figure 2: Single-Cell RNA sequencing of 1-month old MGEOs derived from 3 cell lines

(A) UMAP plot of 1-month-old MGEOs with color coded and numbered clusters. n= 90,631 total cells from 6 samples (2 experimental replicates per hPSC line, 6-8 organoids pooled per sample).

(B) Left: Stacked bar graphs denoting the cluster percent composition for each individual sample included in the UMAP in panel A. Right: Cluster name and color key.

(C) Dot plot showing expression of markers of interest by cell cluster. Circle size denotes percent of cells within a given cluster that expresses the gene of interest. Dot color

indicates average expression level relative to other clusters. Dots were included for all genes that contained greater than 1 percent of cells in a cluster. All cells with >0 expression levels were included in the analysis.

(D) Individual UMAP plots of selected genes. Color gradient denotes expression levels from none (light gray) to highest (dark purple) as depicted by the scale on the right of each plot.

Abbreviations: GE: Ganglionic Eminences; MGE: Medial Ganglionic Eminence; IN: Interneurons; POA: Preoptic area; CGE: Caudal Ganglionic Eminence; LGE: Lateral Ganglionic Eminence; NPC: Neural Progenitor Cell; Cycling Projen: Cycling Progenitors.

Figure 3. MGEOs generate human MGE-derived cell-types

(A) RT-qPCR of 1-, 2- and 3-month MGEOs shows expected mRNA transcript expression of GABAegic, potassium channel, and MGE-derived markers. n≥5 differentiations between 3 cell lines, graphed as average fold change (ΔΔCT) ± SEM, normalization to GAPDH and relative to average iPSC baseline. Shapes denote cell line and color indicates time point (triangle: 2E, circle: 79B, diamond: H9; gray: 1-month, purple: 2-month, orange: 3-month).

(B-D) Immunostaining for cell type-specific markers in 3-month MGEOs. Dashed boxes in B and C denote regions of interest (ROI) shown to the right of each respective image.

(E) Representative images of immunostaining for parvalbumin (PV, green) at 3-, 4-, 6- and 8-months (mo) *in vitro* shows robust PV expression in MGEOs from 4 months onwards. Nuclei are shown in blue with bisbenzimide staining. Dashed boxes denote ROI shown at higher magnification (inset).

(F) Quantification of PV expression as percentage (%) of organoid area ± SD. n=5-8 organoids per timepoint, from n= 2-3 differentiations / cell-line. One way ANOVA with Dunnett's T3 multiple comparisons post hoc test. P= 0.0036 (**).

(G) Immunostaining of 6-month organoids shows colocalization of PV (green) and MEF2C (red), bisbenzimide staining in blue. Dashed box denotes ROI shown at right.

(H) Immunostaining of 3-month (left) and 8-month (right) MGEOs shows that the voltage-gated potassium channel $K_v3.1$ (green) is expressed in MEF2C+ (red) cells at 8

months. Dashed boxes are shown to the right of each image as higher-magnification views of individual red and green channels and also merged with bisbenzimide nuclear stain (DNA, blue).

(I) Immunostaining of 6-month MGEOs shows PV (green) co-expressed with the perineuronal net marker WFA (red). Dashed boxed area is shown on the right as higher-magnification views of individual red and green channels and also merged with bisbenzimide nuclear stain (blue).

(J) Confocal imaging of PV basket cell-specific AAV1-BiPVe3-dTom virus expression in live-imaged 6-month-old MGEOs reveals complex morphologies of putative PV basket cells.

Figure 4: scRNA-seq analysis of 3-month MGEOs reveals MGE specificity

(A) UMAP plot shows 10 clusters from six 3-month-old MGEO samples, 2 differentiations per cell line, with clusters color-coded and numbered. Middle: bar graphs denote the percentages of cells within each sample that correspond to each cluster shown on the UMAP. Each sample contains cells from 4-6 pooled organoids, with samples 1 & 2 derived from H9 (female, hESC-derived), samples 3 & 4 from 79B (female, blood-derived), and samples 5 & 6 from 2E (male, foreskin fibroblast-derived) hPSC lines. Right: Legend of cluster identities by number and color.

(B) Average percentage of cells in each cluster by cell line (2 differentiations per line).

(C) Dot plots showing expression of markers of interest by cell cluster. Circle size denotes the percentage of cells that express the gene of interest within a given cluster, while dot color indicates average expression level relative to all other clusters. Analysis parameters and abbreviations are the same as in Figure 2C.

(D) Individual UMAP plots of selected genes. Color gradients (at the right of each plot) denote a range from no expression (light gray) to highest expression (dark purple).

Figure 5. MGEOs transcriptome closely resembles the developing human MGE

(A) UMAP plot of human GW9-18 single-cell RNA-sequencing data from Shi et al., 2021, with color-coded regional and cell type clustering.

(B) Integrated UMAP plot of scRNAseq data from 3-month MGEOs (orange) compared to human fetal GEs from gestational weeks (GW) 9-18 (Shi et al. 2021. Human fetal MGE cluster: Blue; non-MGE clusters: grey). Insets show the MGEO cluster and human MGE cluster alone.

(C) Principal component analysis (PCA) of 3-month MGEO scRNA-seq data (orange dot) compared to human fetal GE scRNA-seq clusters (gestational weeks 9–18; Shi et al., 2021, black dots) shows that MGEOs are most similar to the human MGE cluster.

(D) UMAP showing 3-month MGEO cell type clusters integrated with human GW9-18 fetal GEs (Shi et al., 2021; in gray). MGEO cell clustering and colors as in Figure 4.

(E) Heat map of Pearson correlation coefficients for comparison of 3-month MGEO neuronal clusters 1-7 (columns, numbered as in panel D and Figure 4) with Shi et al. 2021 human fetal MGE subclusters (rows).

(F) Heat map comparing the average percentage of cells expressing selected gene markers for MGE, LGE, CGE, and preoptic area/hypothalamus (POA/Hypo) across single-cell RNA-sequencing datasets from 3-month MGEOs, human fetal MGE (Shi et al., 2021; gestational weeks 9–18), and other subpallial organoids of similar timepoints (Xiang et al., 2017; Birey et al., 2017).

(G) Integrated UMAP of 3-month MGEO and human fetal GE scRNA-seq data, as shown in panels B and D. Developmental age clusters from Shi et al. are depicted in shades of blue, while 3-month MGEO cells are colored by cell line (red: H9; green: 79B; yellow: 2E). Insets display human fetal cells (left) and MGEO cells (right) separately.

(H) Heatmap of PCA Euclidean distances comparing each 3-month MGEO cell line to human fetal gestational developmental ages (GW 9, 12, 16, and 18) shows 3-month MGEOs are, on average, closest to human developmental timepoints GW12-16.

Figure 6: MGEO-derived neurons rapidly migrate in 2D and 3D assays, and they integrate within dorsal cortical organoids in assembloids

(A) Diagram of 2D migration assay.

(B) Images of MGEOs at 32 hours post-plating (hr pp) at 10 DIV, and (B') 0, 12, and 24 hr pp at 21 DIV on ECM (Geltrex, 1:50). Also see **supplemental video S1** for a representative timelapse video of migrating progenitors.

(C) Confocal images of a MGEO fixed 3 days post plating and immunolabeled for MAP2ab (red) and LHX6 (green) show that migrated cells are MGE-derived neurons. Bisbenzimide (DNA) in blue. Boxed region of upper left image is shown at higher magnification in the other panels.

(D) Schematic of assembloid protocol, involving viral labeling at 48 DIV, fusion at 56 DIV, and subsequent live confocal microscopy from 24 hours to 15 days post fusion (DPF).

(E-F) Images from representative MGEO-CO assembloids at 4 (E) or 5 and 10 (F) DPF. mDLX-GFP (green) virus labels GABAergic cells originating from the MGEO, whereas tdTomato (red) labels cortical organoid progenitors and putative excitatory neurons. See **supplementary video S2** for a video of this migration in a live assembloid taken 5 DPF.

(G) Quantification of migration of mDLx-GFP+ virally labeled MGEO interneurons into COs at 24 hours, 3-5 days, and 10-15 DPF. Percentage area of GFP expression in the CO organoid area ± standard deviation (SD) is shown. Points represent single organoid replicates (n≥4), with the point shape denoting the cell line used (triangle: 2E, circle: 79B, diamond: H9).

(H) Timelapse live imaging of a mDLX-GFP-labeled MGEO interneuron within the CO region of a 2E MGEO-CO assembloid shows characteristic interneuron leading edge branching movement patterns. Time is listed as hr:min. The white arrow denotes the neuronal soma, and the yellow arrowhead points to branching of the leading process. Also see **supplementary video S3**.

(I) Confocal image of an MGEO-CO assembloid at 6 months shows full fusion into a single spherical structure. The boxed area in the left panel is expanded in the right panels. Labeling with mDLX-GFP (green) and tdTomato (red) is as described in D-F.

(J) Immunostaining of a 7.5 month MGEO:CO assembloid shows expression of GABAergic post- and pre-synaptic markers Gephyrin (green) and vGAT (red), respectively, on a CAG-tdTom CO neuron (pseudocolored blue). Boxed area in the left panel is shown at higher magnification at right, with white arrowheads in the merged image showing closely apposed vGAT+ and Gephyrin+ puncta.

(K) Immunolabeling of a 6-month MGEO:CO assembloid shows VGAT puncta (green) localized along an Ankyrin G (AnkG)-positive axon initial segment (white).

Figure 7. MGEO-CO assembloids form functional excitatory and inhibitory synapses, and display increased complexity of network activity and fast-spiking units over time

(A) Diagram of organoid slicing and whole-cell patch clamp recordings of MGEO-CO assembloid excitatory and inhibitory neurons.

(B) Representative traces showing spontaneous (B) and evoked (B') repetitive firing of mDLX-GFP+ (MGEO-derived) neurons in MGEO-CO assembloid slices at 204 DIV. Repetitive AP firing was evoked from resting membrane potential by injection of 1500 ms pulse currents of 20 pA.

(C) Representative trace of spontaneous excitatory postsynaptic currents (sEPSCs) recorded from an mDLX-GFP+ (MGEO-derived) neuron within an MGEO-CO assembloid slice at 204 DIV at a holding potential of -70 mV.

(D) Representative trace of spontaneous inhibitory postsynaptic currents (sIPSCs) recorded from a CAG-tdT+ (CO-derived) neuron in the same assembloid slice as (C). (D') sIPSC were recorded at a holding potential of -70 mV in the presence of 6-cyano-7-nitroquinoxaline-2,3-dione (CNQX, 10 µM) and amino-5-phosphonopentanoic acid (APV, 50 - 100 µM) in the external solution to block glutamate receptor-mediated synaptic responses.

(E) Brightfield image of a 6 month MGEO-CO assembloid cultured in suspension and acutely plated on an MEA plate for recording.

(F) Representative MEA voltage traces from 3 electrodes taken from n = 2 representative MGE-CO assembloid recordings shown over a 2 s window (left) and a 5 min window (right).

(G) Cumulative distribution of maximum firing rates between DIV-140 CO-CO (gray) and MGEO-CO (light blue) assembloids. n=3 each from 2 cell lines with 62 putative units per assembloid type. Two-tailed Kolmogorov-Smirnov test, P = 0.0056.

(H) Representative raster plots of putative units in MGEO-CO assembloids at different maturation stages: DIV-140 (n=3), DIV-212 (n=4-6), and DIV-235 (n = 4-6) MGE-CO assembloids from 2 cell lines.

(I-J) Cumulative distribution of maximum firing rates (I) and burst counts (J) across

maturation stages (DIV-140, DIV-212, and DIV-235) using same samples as in H. Two-tailed Kolmogorov-Smirnov test, DIV 140 vs 212: (I) KS=0.5010, *P*=2.3247e-07, (J) KS=0.5062, P=1.6290 x10^{-7}. DIV 140 vs 235: (I) KS Stat=0.4597, *P*=4.1009e-06, (J) KS Stat=0.5123, P=1.5173 x10^{-7} DIV 212 vs 235: (I) KS Stat=0.1350, p-value=8.1858e-01, (J) KS=0.1404, P=0.77593. N=38-62 putative units/3-5 assembloids per developmental window.

(K) Electrode-matched representative voltage traces from a 5 min recording before (gray, top) and after (black, bottom) application of 10 µM bicuculline.

(L) Firing rate per burst of putative units. Boxplots display the median, 25th and 75th percentiles (box edges), whiskers extending to the most extreme data points, and individual outliers plotted separately. Two-tailed Mann-Whitney U=*113, P*= 0.007, Pre Bic treatment: N= 9-11 putative units/3 MGEO-COs, During Bic treatment: 8-10 putative units/2 MGEO-COs.

(M) Representative voltage trace with corresponding raster plots of three putative units recorded during a network burst. Orange represents a putative regular-spiking unit (RS1), while brown (FS1) and beige (FS2) represent putative fast-spiking units.

(N) Quantification from panel (M): histogram distribution of putative FS vs. RS units pooled from n = 10 assembloids across at least two independent differentiations each from 2 different cell lines. (N') representative voltage traces of putative RS and FS units aligned to the trough. The mean trough-normalized waveforms of each unit are overlaid, showing trough to peak (TTP) measurements and non-overlapping RS and FS waveforms. MEA data shown is pooled from 2-4 independent differentiations.

Supplementary Video S1: Video shows rapid cell migration from a 21 DIV MGEO onto thin Geltrex in 2D migration assay. Phase images were taken every 5 minutes (timestamps at bottom right, listed as hrs:mins:seconds) using an Incucyte S3 Live Cell Analysis System. Also see main figure 6.

Supplementary Video S2: Video of MGEO interneuron migration into cortical organoid 5-days post fusion. Live confocal imaging of a 79B assembloid fused at 56

DIV shows migration of AAV1-mDLX-GFP labeled MGEO interneurons (green) migrating into an AAV-CAG-tdTom labeled SOSR-CO (red).

Supplemental Video S3: MGEO-derived interneurons show leading-edge branching migratory movement patterns. Time-lapse video of AAV-mDLX-GFP-labeled MGEO interneuron migration one day post fusion to a cortical organoid (CO) labeled with AAV-CAG-tdTom. Arrows track the soma of two neurons throughout the 4 hour time-course (time is listed as hr:min at top left). Organoids were derived from 2E male iPSC line and fused at 56 DIV. Also see **Main Figure 6H.**

Supplementary Figure S1: Exposure to 1uM SAG and 2uM XAV939 from days 6-14 results in SOSRS with mixed regional marker expression

(A) Schematic of the previous ventralization protocol used to generate organoids analyzed by scRNA-seq in panels B–D.

(B) UMAP of scRNAseq data from two organoids (“A” and “B”) show relatively equal of cells across the integrated dataset.

(C) UMAP from panel B labeled by cluster numbered and color-coded by cluster identity.

(D) Feature plots showing expression of select gene markers. Color scale bar to the right of each plot indicate gene expression levels per cell, from no (blue) to high (orange).

Supplementary Figure S2: Further validation of the MGE regional specificity of MGEOs

(A, B) Immunostaining of PAX6 in 1 month (mo) MGEOs (A) and SOSR-COs (B).

(C) 1 month MGEOs immunostained with SHH and RAX. Bisbenzimide nuclear stain (DNA) is in blue for all images.

(D) Immunostaining for NKX2.1 (green) and OLIG2 (red) at 1 month (left) and 3 months (right) shows co-expression at early timepoint, but not the latter. Boxed region indicates areas of magnification displayed on the right of each image.

(E) Quantification of D. Pie charts showing the percent of OLIG2 area that co-localizes with NKX2-1 (yellow) vs does not co-localize (red) at 1 month and 3 months.

Supplementary Figure S3: MGEO interneuron subtype expression

(A) UMAP Feature plots showing expression of key GABAergic and lack of Glutamatergic and CGE cell types in 3-month MGEOs.

(B) UMAP Feature plots of CALB2+ cells that co-express known CGE markers NR2F2 and SP8. Lack of co-expression of these markers in the 3-month MGEO CALB2+ population indicates that CALB2 cells do not have a CGE identity.

(C) Heat map comparing the average percentage of cells expressing key GABAergic cell markers across single-cell RNA-sequencing datasets from 3-month MGEOs, human fetal MGE (Shi et al., 2021; gestational weeks 9–18), and other subpallial organoids of similar timepoints (Xiang et al., 2017; Birey et al., 2017).

(D) Stacked violin plots of MGE lineage markers grouped by MGEO age and cluster.

(E) Venn diagram of gene co-expression between highly represented GABAergic cell types in 3-month MGEOs.

Supplemental Figure S4 : AMD3100 treatment reduces MGEO GABAergic interneuron migration.

(A) Schematic diagram showing SDF-1 binding to CXCR4 receptors to promote migration of MGE-derived GABAergic interneurons into the cortex.

(B) scRNA-seq feature plots show *CXCR4*, *CXCL12* (SDF-1) and *ACKR3* (CXCR7) expression in MGEOs at 1 mo.

(C) Protocol diagram for 2D migration assay with 100 nM treatment of the CXCR4 antagonist AMD3100.

(D) Images of a representative MGEO for each AMD3100 experimental condition at 48 hours post plating (hr pp) at 30 DIV.

(E) Quantification of migrated neuron area ± SD in MGEOs 48 hrs pp for 2D migration assay. 8 organoids from 2 differentiations were used per condition and statistical significance was assessed using One-Way ANOVA with repeated measures and Tukey’s multiple comparisons correction. Adjusted P-value for control vs acute

AMD3100 treatment conditions was 0.1130 (ns), while chronic condition was statistically significant at 0.0036 (**).

(F) Quantification of mDLX-GFP MGEO interneuron area migrated into CO organoid area 48 hours post MEGEO-CO fusion, with ±100 nM AMD3100 started from 1 day post fusion, shows a similar trend as in 2D migration assay. Student T-test statistical comparison between control and AMD3100 treatment organoids (n=4 per group) had an adjusted p-value of 0.0875.

Supplementary Figure S5: Validation of mDLX-GFP specificity and characterization of interneurons in MGE-CO assembloids

(A) Immunostaining of 4-mo MGEOs shows AAV1-mDLX-GFP virus labeled cells (green) co-express GABA (pink). Bisbenzimide nuclear stain (DNA) is in blue.

(B) mDLX-GFP-labeled MGEO-derived interneurons in assembloids at 6 months (mo) *in vitro* have bipolar and multipolar morphologies typical of MGE born GABAergic cells.

(C) MGEO-derived interneurons expressing mDLX-GFP on the outer surface of assembloids exhibit extensive process formation by 6 months *in vitro.*

(D) Immunostaining shows PV expression (green) along the periphery of a 9 mo MGEO-CO assembloid. Bisbenzimide nuclear stain is in blue and inset shows a higher magnification image from the boxed region.

(E) Quantification of (D) PV-positive immunolabeling from 9 mo assembloids as percent of organoid area. n=3 assembloids.

(F) Immunostaining of 9 mo MGEO-CO assembloid shows expression of the voltage-gated potassium channel $K_v3.1$ (fuchsia) along the periphery of the assembloid. Inset shows a higher magnification image from the boxed region.

Supplementary Figure S6: Complexity of MEA network activity

(A) Representative continuous 5-minute MEA recording from a 235-day assembloid showing complexity of network bursting activity.

Supplementary Figure S7: Expression of neurodevelopmental disorder genes in MGEOs

(A) Complex gene expression heat map grouped by cell type and timepoint showing average expression of a group of genes commonly implicated in various neurodevelopmental disorders.

Graphical Abstract

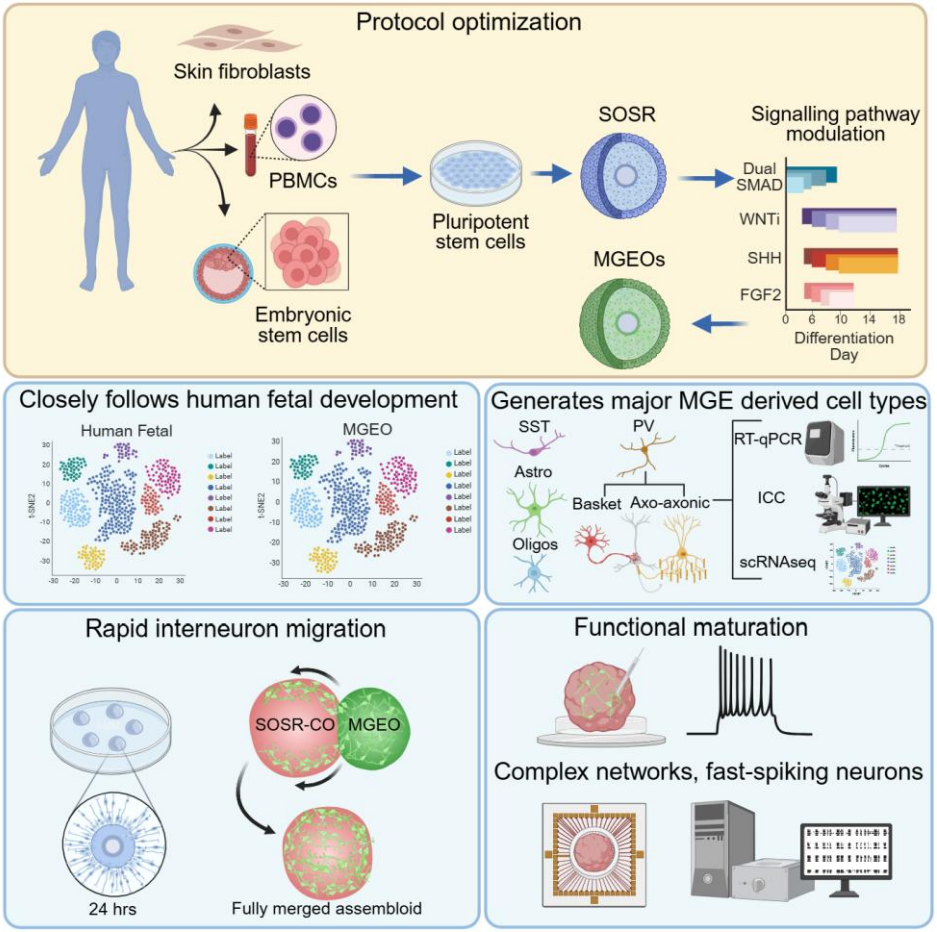

Figure 1

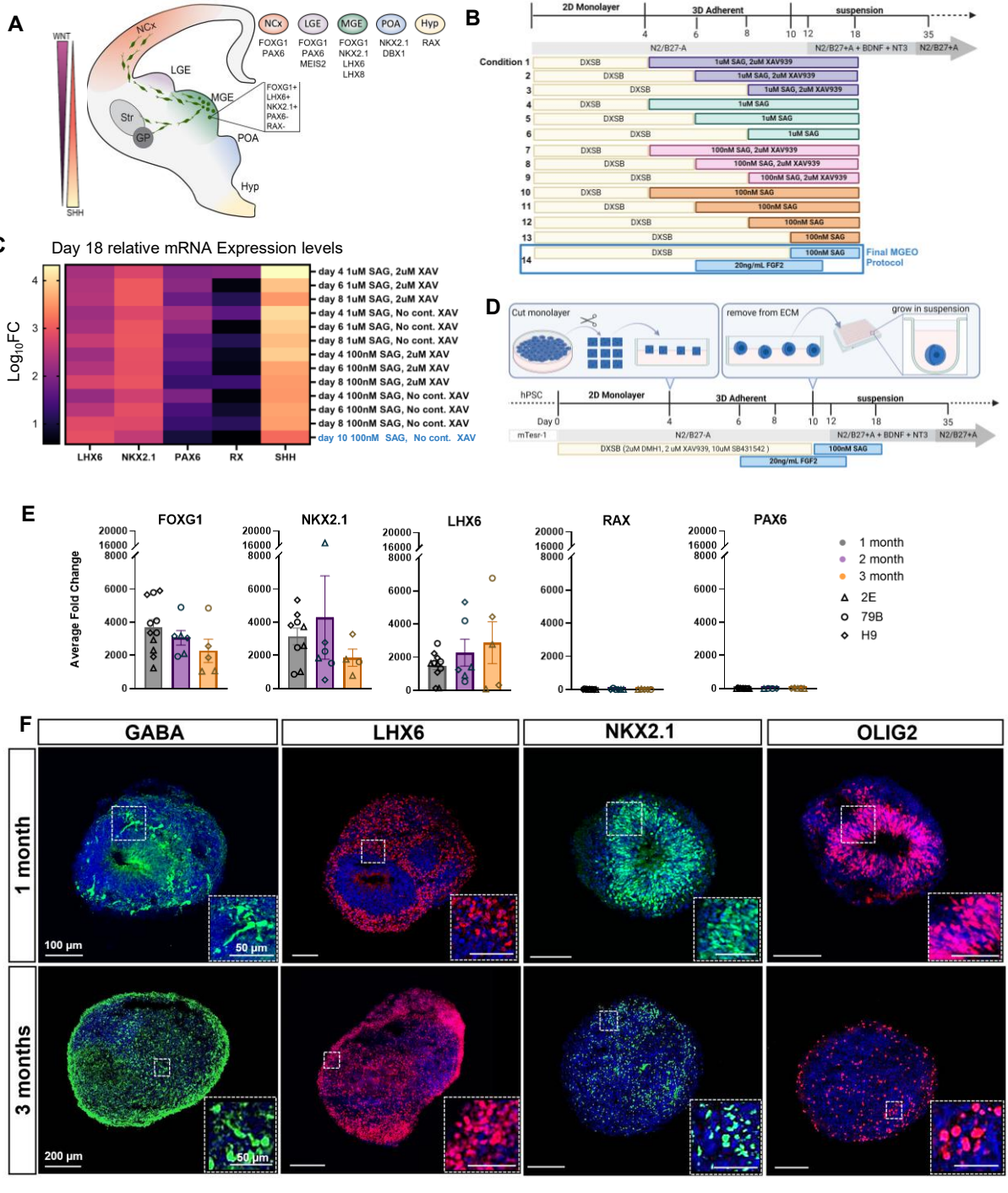
A
WNT
SHH
NCx
LGE
MGE
Str
GP
POA
Hyp
FOXG1+
LHX6+
NKX2.1+
PAX6-
RAX-
NCx FOXG1 PAX6
LGE FOXG1 PAX6 MEIS2
MGE FOXG1 NKX2.1 LHX6 LHX8
POA NKX2.1 DBX1
Hyp RAX
B
2D Monolayer
3D Adherent
suspension
4 6 8 10 12 18 35
N2/B27-A
N2/B27+A + BDNF + NT3
N2/B27+A
Condition 1
DXSB
1uM SAG, 2uM XAV939
1uM SAG
100nM SAG, 2uM XAV939
100nM SAG
20ng/mL FGF2
Final MGEO Protocol
C
Day 18 relative mRNA Expression levels
Log10FC
day 4 1uM SAG, 2uM XAV
day 6 1uM SAG, 2uM XAV
day 8 1uM SAG, 2uM XAV
day 4 1uM SAG, No cont. XAV
day 6 1uM SAG, No cont. XAV
day 8 1uM SAG, No cont. XAV
day 4 100nM SAG, 2uM XAV
day 6 100nM SAG, 2uM XAV
day 8 100nM SAG, 2uM XAV
day 4 100nM SAG, No cont. XAV
day 6 100nM SAG, No cont. XAV
day 8 100nM SAG, No cont. XAV
day 10 100nM SAG, No cont. XAV
LHX6 NKX2.1 PAX6 RX SHH
D
Cut monolayer
remove from ECM
grow in suspension
hPSC
Day 0
mTesr-1
DXSB (2uM DMH1, 2 uM XAV939, 10uM SB431542)
E
FOXG1
NKX2.1
LHX6
RAX
PAX6
Average Fold Change
1 month
2 month
3 month
2E
79B
H9
F
GABA
LHX6
NKX2.1
OLIG2
1 month
3 months
100 µm
50 µm
200 µm

Figure 2

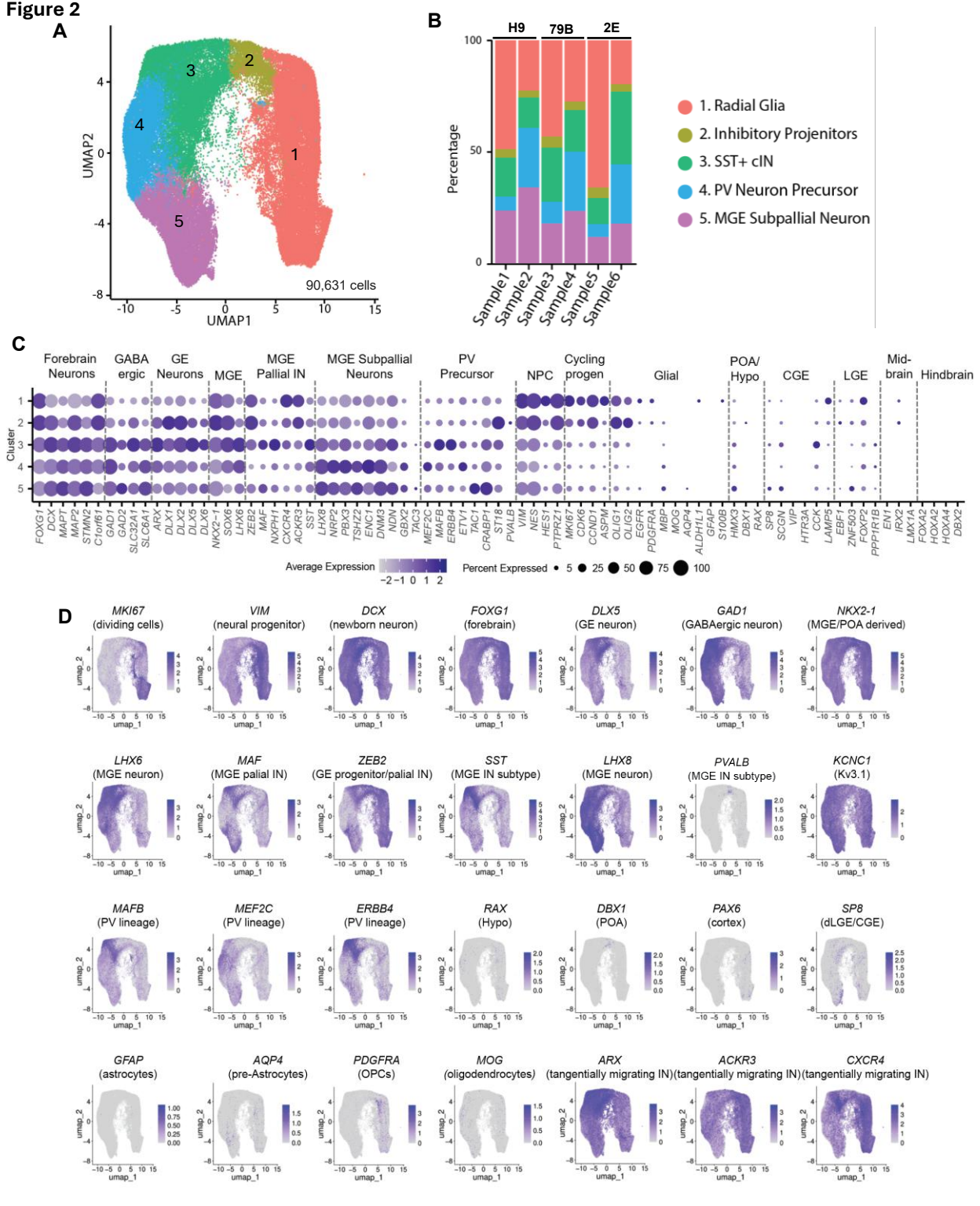
A
UMAP2
UMAP1
90,631 cells
1
2
3
4
5
B
H9
79B
2E
Percentage
Sample1
Sample2
Sample3
Sample4
Sample5
Sample6
1. Radial Glia
2. Inhibitory Projenitors
3. SST+ cIN
4. PV Neuron Precursor
5. MGE Subpallial Neuron
C
Forebrain Neurons
GABA ergic
GE Neurons
MGE
MGE Pallial IN
MGE Subpallial Neurons
PV Precursor
NPC
Cycling progen
Glial
POA/ Hypo
CGE
LGE
Mid-brain
Hindbrain
Cluster
FOXG1 DCX MAPT MAP2 STMN2 C1orf61 GAD1 GAD2 SLC32A1 SLC6A1 ARX DLX1 DLX2 DLX5 DLX6 NKX2-1 SOX6 LHX6 ZEB2 MAF NXPH1 CXCR4 ACKR3 SST LHX8 NRP2 PBX3 TSHZ2 ENC1 DNM3 NDN GBX2 TAC3 MEF2C MAFB ERBB4 ETV1 TAC1 CRABP1 ST18 PVALB VIM NES HES1 PTPRZ1 MKI67 CDK6 CCND1 ASPM OLIG1 OLIG2 EGFR PDGFRA MBP MOG AQP4 ALDH1L1 GFAP S100B HMX3 DBX1 RAX SP8 SCGN VIP HTR3A CCK LAMP5 EBF1 ZNF503 FOXP2 PPP1R1B EN1 IRX2 LMX1A FOXA2 HOXA2 HOXA4 DBX2
Average Expression
Percent Expressed
D
MKI67 (dividing cells)
VIM (neural progenitor)
DCX (newborn neuron)
FOXG1 (forebrain)
DLX5 (GE neuron)
GAD1 (GABAergic neuron)
NKX2-1 (MGE/POA derived)
LHX6 (MGE neuron)
MAF (MGE palial IN)
ZEB2 (GE progenitor/palial IN)
SST (MGE IN subtype)
LHX8 (MGE neuron)
PVALB (MGE IN subtype)
KCNC1 (Kv3.1)
MAFB (PV lineage)
MEF2C (PV lineage)
ERBB4 (PV lineage)
RAX (Hypo)
DBX1 (POA)
PAX6 (cortex)
SP8 (dLGE/CGE)
GFAP (astrocytes)
AQP4 (pre-Astrocytes)
PDGFRA (OPCs)
MOG (oligodendrocytes)
ARX (tangentially migrating IN)
ACKR3 (tangentially migrating IN)
CXCR4 (tangentially migrating IN)
umap_1
umap_2

Figure 3

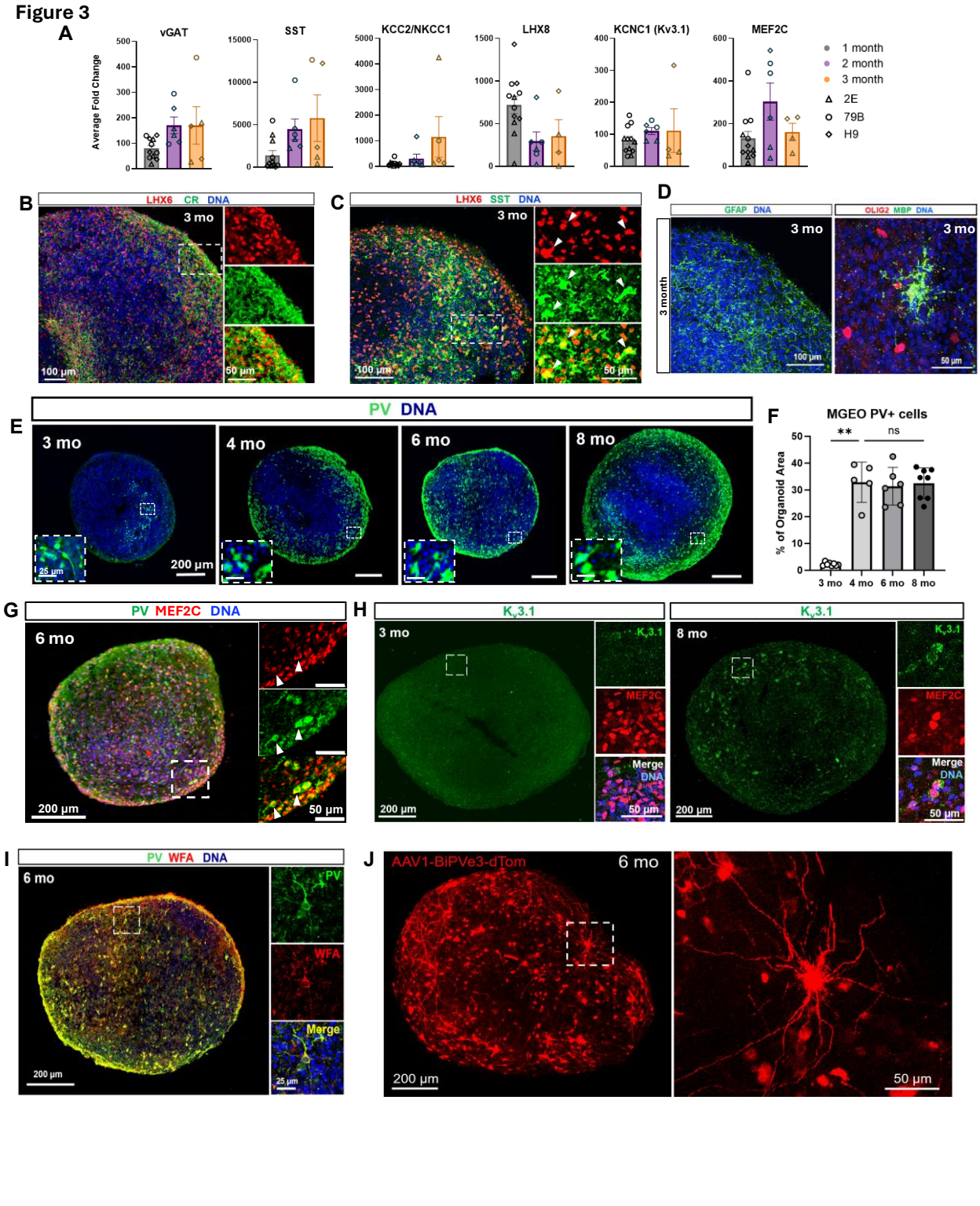
A
vGAT
SST
KCC2/NKCC1
LHX8
KCNC1 (Kv3.1)
MEF2C
Average Fold Change
1 month
2 month
3 month
2E
79B
H9
B
LHX6 CR DNA
3 mo
100 µm
50 µm
C
LHX6 SST DNA
3 mo
100 µm
50 µm
D
GFAP DNA
OLIG2 MBP DNA
3 mo
3 month
100 µm
50 µm
E
PV DNA
3 mo
4 mo
6 mo
8 mo
25 µm
200 µm
F
MGEO PV+ cells
**
ns
% of Organoid Area
3 mo
4 mo
6 mo
8 mo
G
PV MEF2C DNA
6 mo
200 µm
50 µm
H
Kv3.1
3 mo
8 mo
MEF2C
Merge
DNA
200 µm
50 µm
I
PV WFA DNA
6 mo
PV
WFA
Merge
200 µm
25 µm
J
AAV1-BiPVe3-dTom
6 mo
200 µm
50 µm

Figure 4

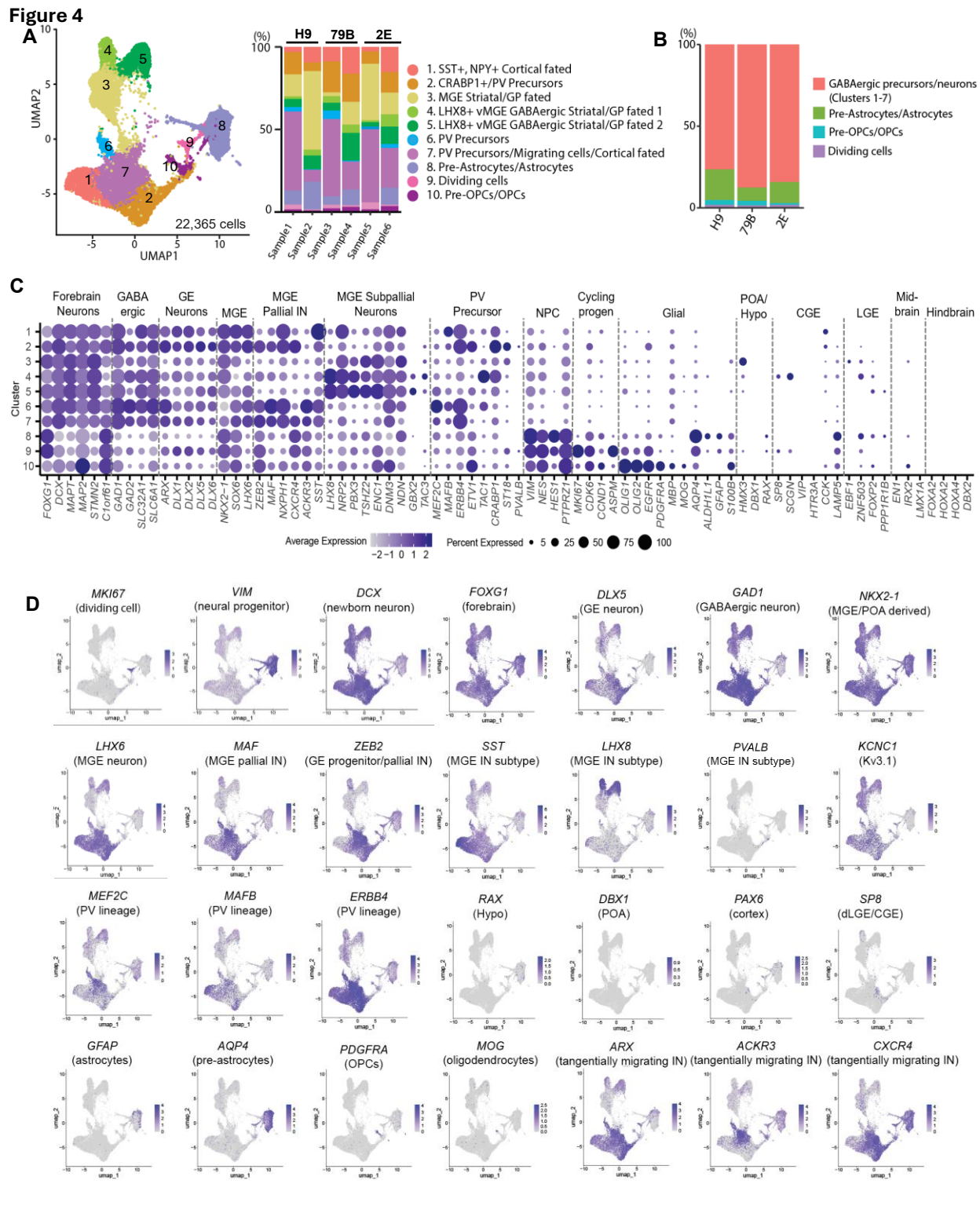
A
UMAP2
UMAP1
22,365 cells
H9
79B
2E
(%)
1. SST+, NPY+ Cortical fated
2. CRABP1+/PV Precursors
3. MGE Striatal/GP fated
4. LHX8+ vMGE GABAergic Striatal/GP fated 1
5. LHX8+ vMGE GABAergic Striatal/GP fated 2
6. PV Precursors
7. PV Precursors/Migrating cells/Cortical fated
8. Pre-Astrocytes/Astrocytes
9. Dividing cells
10. Pre-OPCs/OPCs
Sample1
Sample2
Sample3
Sample4
Sample5
Sample6
B
GABAergic precursors/neurons (Clusters 1-7)
Pre-Astrocytes/Astrocytes
Pre-OPCs/OPCs
Dividing cells
C
Forebrain Neurons
GABA ergic
GE Neurons
MGE
MGE Pallial IN
MGE Subpallial Neurons
PV Precursor
NPC
Cycling progen
Glial
POA/ Hypo
CGE
LGE
Mid-brain
Hindbrain
Cluster
Average Expression
Percent Expressed
D
MKI67 (dividing cell)
VIM (neural progenitor)
DCX (newborn neuron)
FOXG1 (forebrain)
DLX5 (GE neuron)
GAD1 (GABAergic neuron)
NKX2-1 (MGE/POA derived)
LHX6 (MGE neuron)
MAF (MGE pallial IN)
ZEB2 (GE progenitor/pallial IN)
SST (MGE IN subtype)
LHX8 (MGE IN subtype)
PVALB (MGE IN subtype)
KCNC1 (Kv3.1)
MEF2C (PV lineage)
MAFB (PV lineage)
ERBB4 (PV lineage)
RAX (Hypo)
DBX1 (POA)
PAX6 (cortex)
SP8 (dLGE/CGE)
GFAP (astrocytes)
AQP4 (pre-astrocytes)
PDGFRA (OPCs)
MOG (oligodendrocytes)
ARX (tangentially migrating IN)
ACKR3 (tangentially migrating IN)
CXCR4 (tangentially migrating IN)

Figure 5

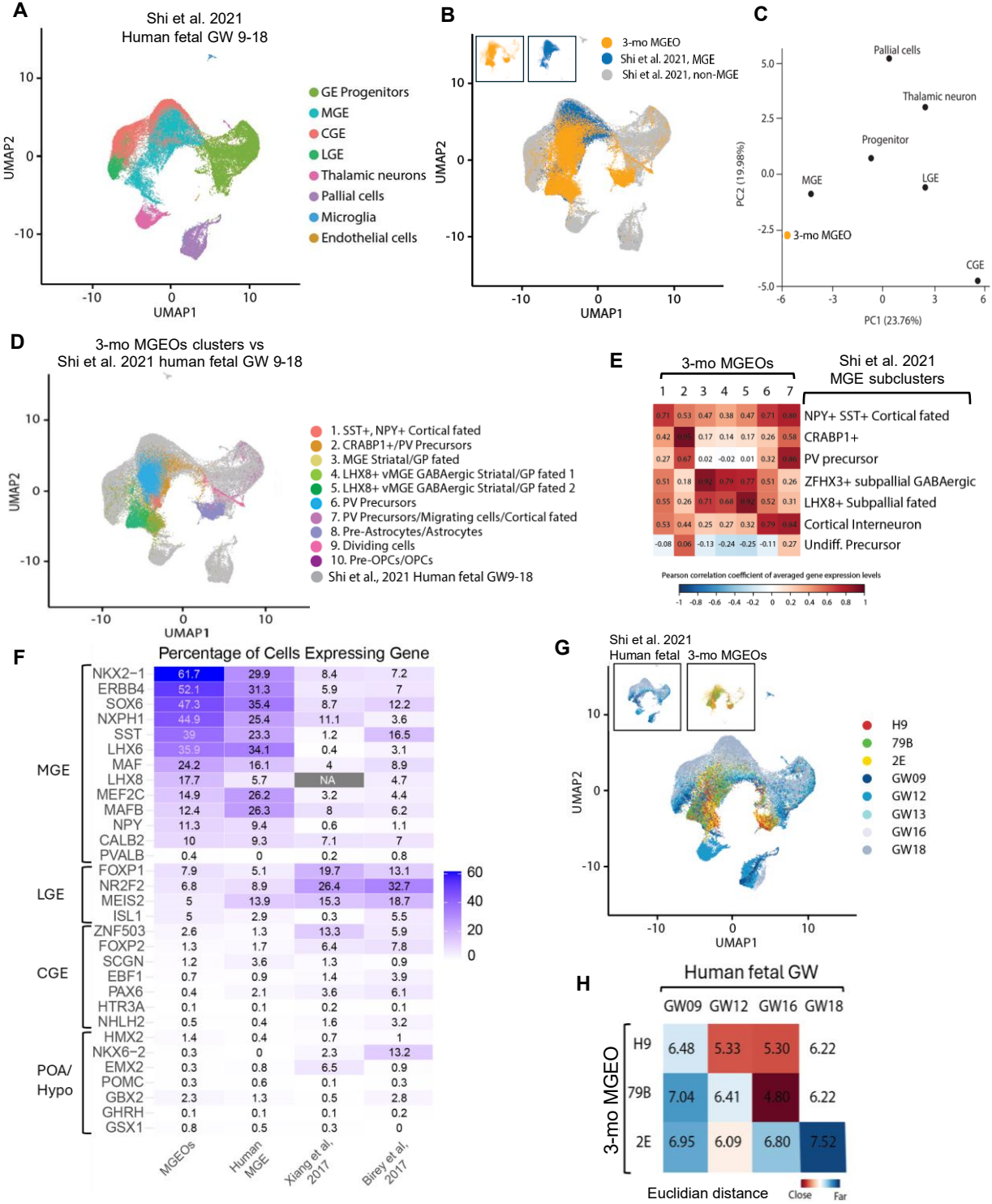
A
Shi et al. 2021
Human fetal GW 9-18
GE Progenitors
MGE
CGE
LGE
Thalamic neurons
Pallial cells
Microglia
Endothelial cells
UMAP1
UMAP2
B
3-mo MGEO
Shi et al. 2021, MGE
Shi et al. 2021, non-MGE
C
Pallial cells
Thalamic neuron
Progenitor
MGE
LGE
3-mo MGEO
CGE
PC1 (23.76%)
PC2 (19.98%)
D
3-mo MGEOs clusters vs
Shi et al. 2021 human fetal GW 9-18
1. SST+, NPY+ Cortical fated
2. CRABP1+/PV Precursors
3. MGE Striatal/GP fated
4. LHX8+ vMGE GABAergic Striatal/GP fated 1
5. LHX8+ vMGE GABAergic Striatal/GP fated 2
6. PV Precursors
7. PV Precursors/Migrating cells/Cortical fated
8. Pre-Astrocytes/Astrocytes
9. Dividing cells
10. Pre-OPCs/OPCs
Shi et al., 2021 Human fetal GW9-18
E
3-mo MGEOs
Shi et al. 2021
MGE subclusters
NPY+ SST+ Cortical fated
CRABP1+
PV precursor
ZFHX3+ subpallial GABAergic
LHX8+ Subpallial fated
Cortical Interneuron
Undiff. Precursor
Pearson correlation coefficient of averaged gene expression levels
F
Percentage of Cells Expressing Gene
MGE
LGE
CGE
POA/
Hypo
NKX2-1 61.7 29.9 8.4 7.2
ERBB4 52.1 31.3 5.9 7
SOX6 47.3 35.4 8.7 12.2
NXPH1 44.9 25.4 11.1 3.6
SST 39 23.3 1.2 16.5
LHX6 35.9 34.1 0.4 3.1
MAF 24.2 16.1 4 8.9
LHX8 17.7 5.7 NA 4.7
MEF2C 14.9 26.2 3.2 4.4
MAFB 12.4 26.3 8 6.2
NPY 11.3 9.4 0.6 1.1
CALB2 10 9.3 7.1 7
PVALB 0.4 0 0.2 0.8
FOXP1 7.9 5.1 19.7 13.1
NR2F2 6.8 8.9 26.4 32.7
MEIS2 5 13.9 15.3 18.7
ISL1 5 2.9 0.3 5.5
ZNF503 2.6 1.3 13.3 5.9
FOXP2 1.3 1.7 6.4 7.8
SCGN 1.2 3.6 1.3 0.9
EBF1 0.7 0.9 1.4 3.9
PAX6 0.4 2.1 3.6 6.1
HTR3A 0.1 0.1 0.2 0.1
NHLH2 0.5 0.4 1.6 3.2
HMX2 1.4 0.4 0.7 1
NKX6-2 0.3 0 2.3 13.2
EMX2 0.3 0.8 6.5 0.9
POMC 0.3 0.6 0.1 0.3
GBX2 2.3 1.3 0.5 2.8
GHRH 0.1 0.1 0.1 0.2
GSX1 0.8 0.5 0.3 0
MGEOs
Human MGE
Xiang et al. 2017
Birey et al. 2017
G
Shi et al. 2021
Human fetal
3-mo MGEOs
H9
79B
2E
GW09
GW12
GW13
GW16
GW18
H
Human fetal GW
GW09 GW12 GW16 GW18
3-mo MGEO
H9 6.48 5.33 5.30 6.22
79B 7.04 6.41 4.80 6.22
2E 6.95 6.09 6.80 7.52
Euclidian distance
Close
Far

Figure 6

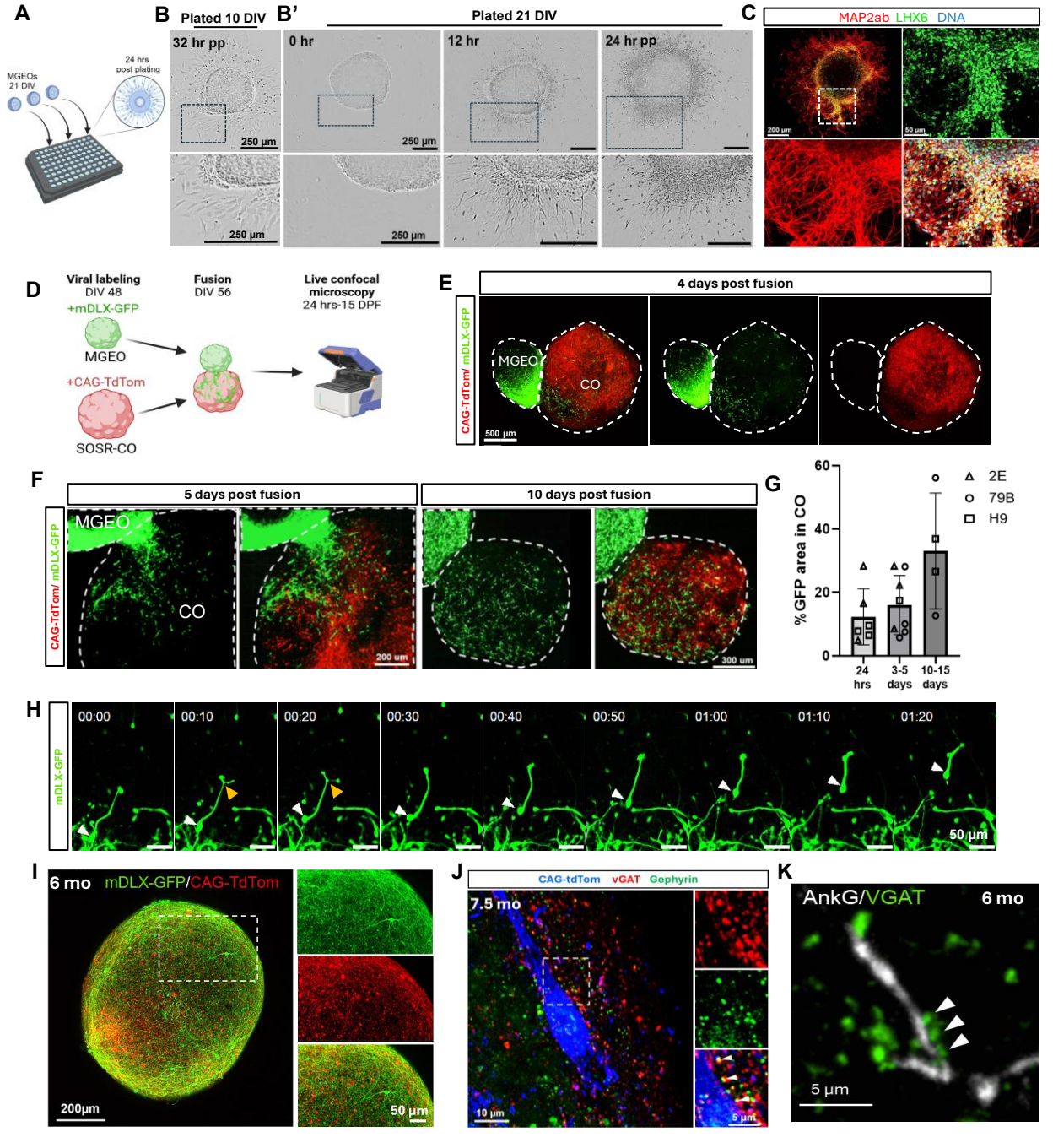
A
MGEOs
21 DIV
24 hrs
post plating
B
Plated 10 DIV
32 hr pp
250 µm
B'
Plated 21 DIV
0 hr
12 hr
24 hr pp
250 µm
C
MAP2ab LHX6 DNA
200 µm
50 µm
D
Viral labeling
DIV 48
+mDLX-GFP
MGEO
+CAG-TdTom
SOSR-CO
Fusion
DIV 56
Live confocal
microscopy
24 hrs-15 DPF
E
4 days post fusion
CAG-TdTom/ mDLX-GFP
MGEO
CO
500 µm
F
5 days post fusion
10 days post fusion
CAG-TdTom/ mDLX-GFP
MGEO
CO
200 um
300 um
G
% GFP area in CO
60
40
20
0
2E
79B
H9
24 hrs
3-5 days
10-15 days
H
mDLX-GFP
00:00
00:10
00:20
00:30
00:40
00:50
01:00
01:10
01:20
50 µm
I
6 mo
mDLX-GFP/CAG-TdTom
200µm
50 µm
J
CAG-tdTom vGAT Gephyrin
7.5 mo
10 µm
5 µm
K
AnkG/VGAT
6 mo
5 µm

Figure 7

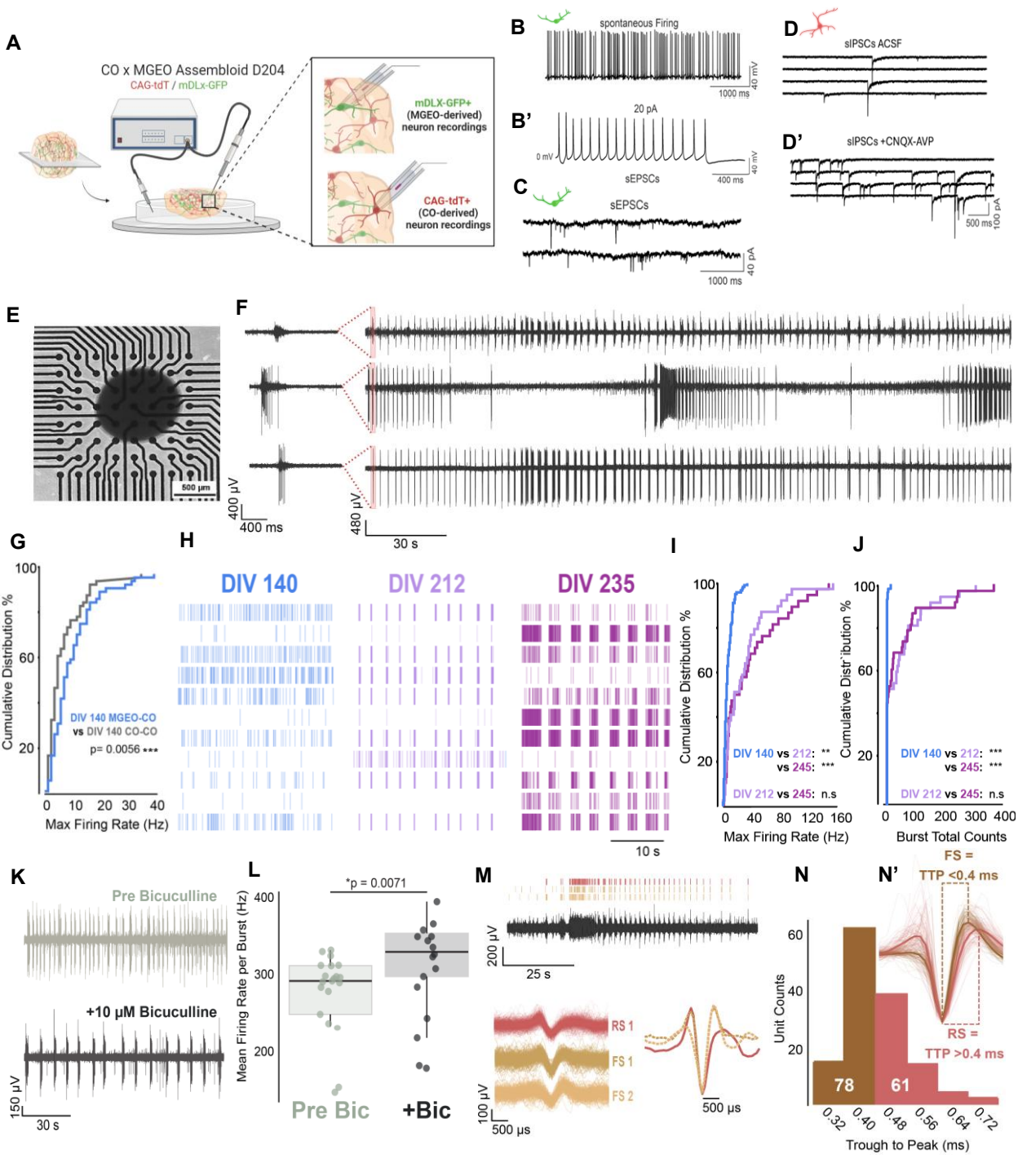
A
CO x MGEO Assembloid D204
CAG-tdT / mDLx-GFP
mDLX-GFP+
(MGEO-derived)
neuron recordings
CAG-tdT+
(CO-derived)
neuron recordings
B
spontaneous Firing
40 mV
1000 ms
B'
20 pA
0 mV
sEPSCs
400 ms
40 mV
C
sEPSCs
40 pA
1000 ms
D
sIPSCs ACSF
D'
sIPSCs +CNQX-AVP
500 ms
100 pA
E
500 µm
F
400 µV
400 ms
480 µV
30 s
G
Cumulative Distribution %
DIV 140 MGEO-CO
vs DIV 140 CO-CO
p= 0.0056 ***
Max Firing Rate (Hz)
H
DIV 140
DIV 212
DIV 235
10 s
I
Cumulative Distribution %
DIV 140 vs 212: **
vs 245: ***
DIV 212 vs 245: n.s
Max Firing Rate (Hz)
J
Cumulative Distribution %
DIV 140 vs 212: ***
vs 245: ***
DIV 212 vs 245: n.s
Burst Total Counts
K
Pre Bicuculline
+10 µM Bicuculline
150 µV
30 s
L
*p = 0.0071
Mean Firing Rate per Burst (Hz)
Pre Bic
+Bic
M
200 µV
25 s
RS 1
FS 1
FS 2
100 µV
500 µs
500 µs
N
N'
FS =
TTP <0.4 ms
RS =
TTP >0.4 ms
Unit Counts
78
61
Trough to Peak (ms)

Supplement Figure S1

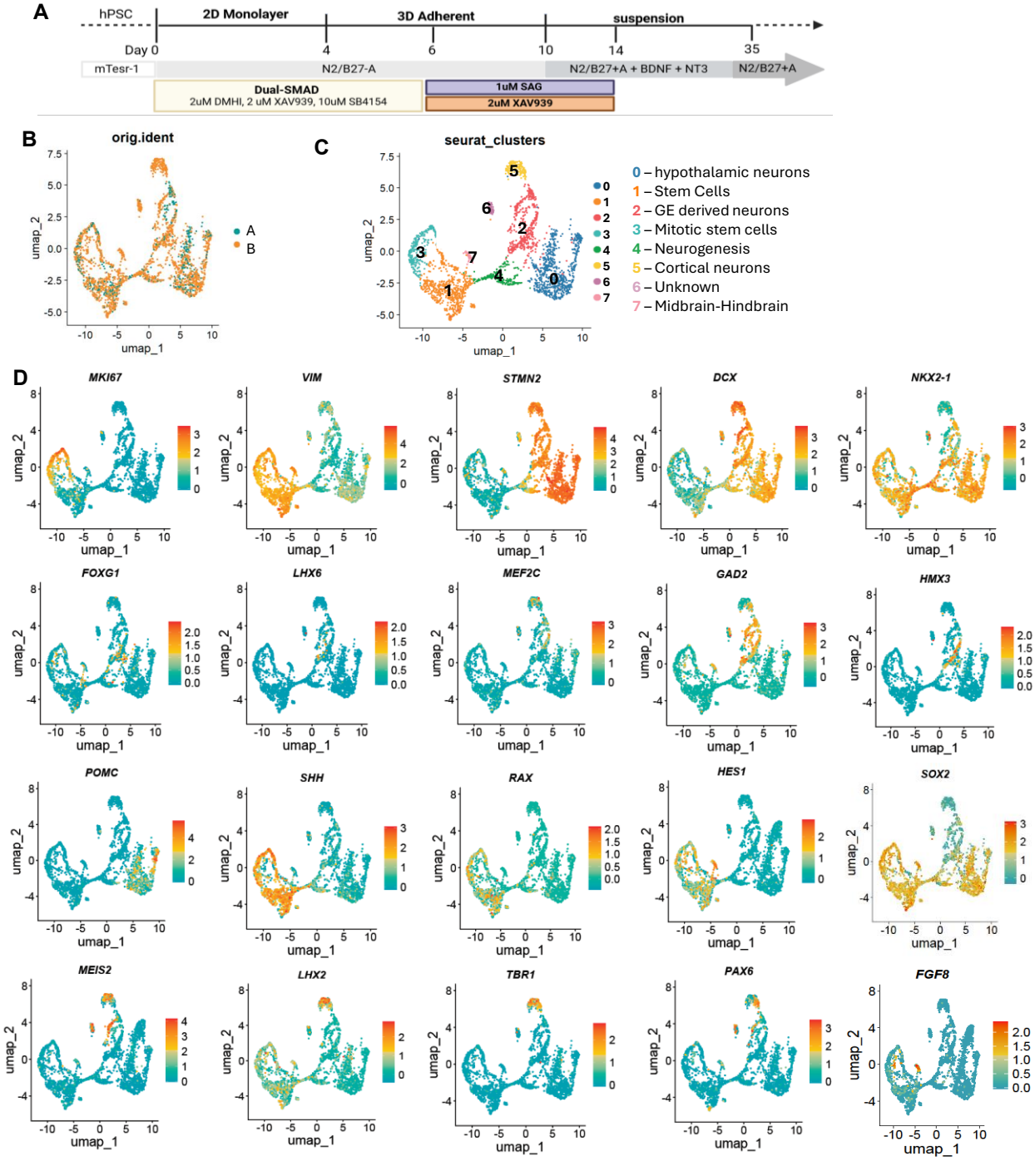

Supplemental Figure S2

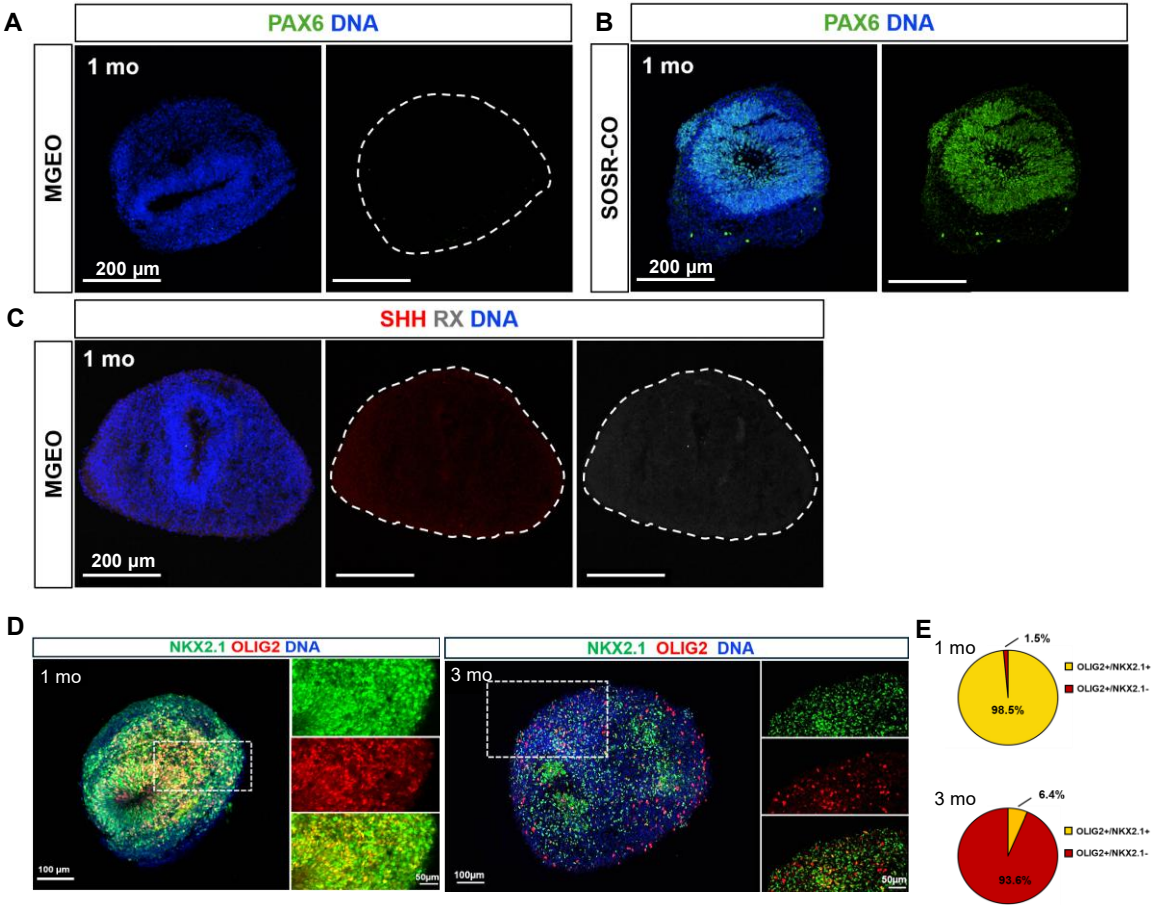

Supplemental Figure S3

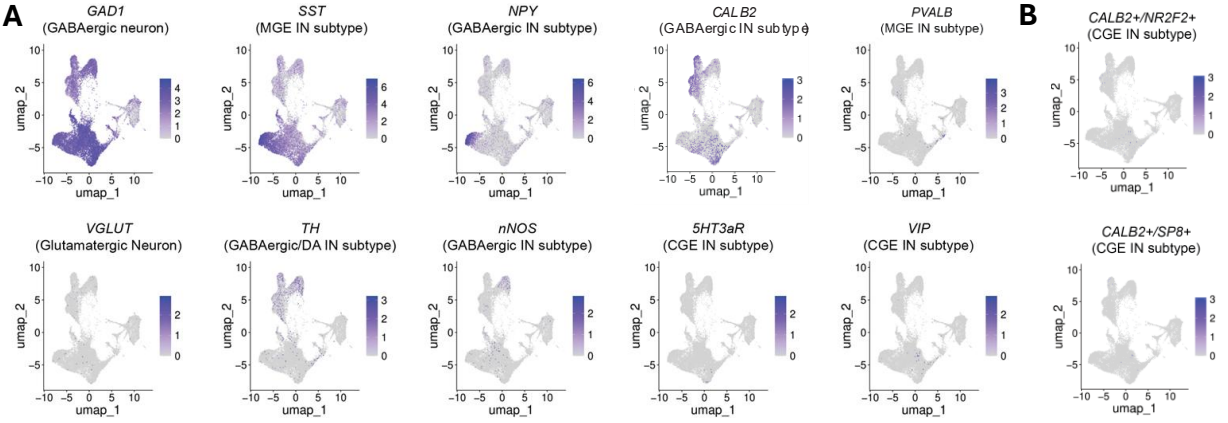

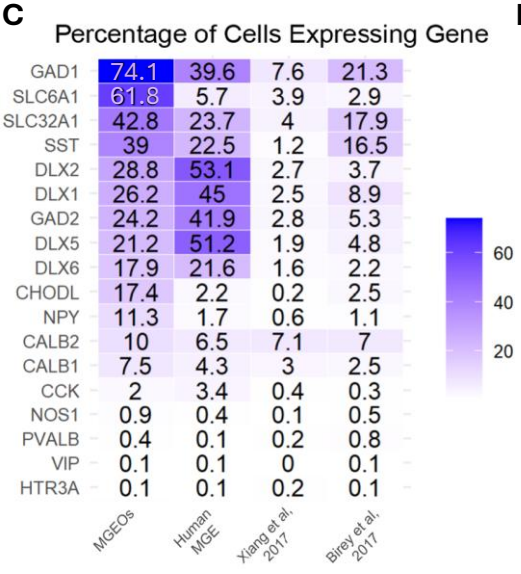

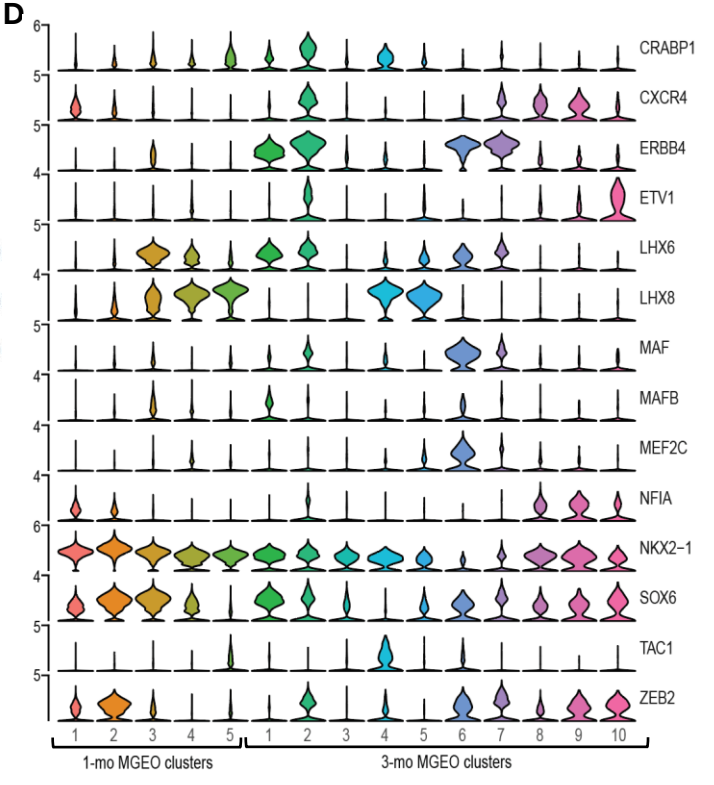

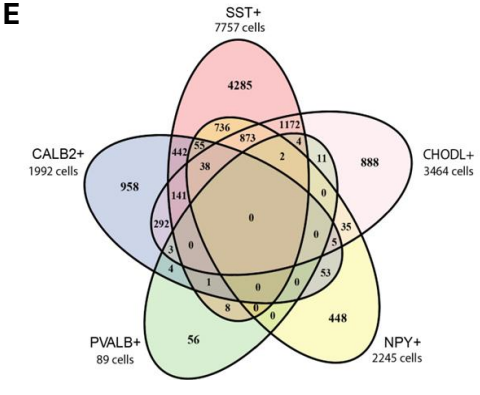

3-mo MGEO Interneuron Subtypes

Supplemental Figure S4

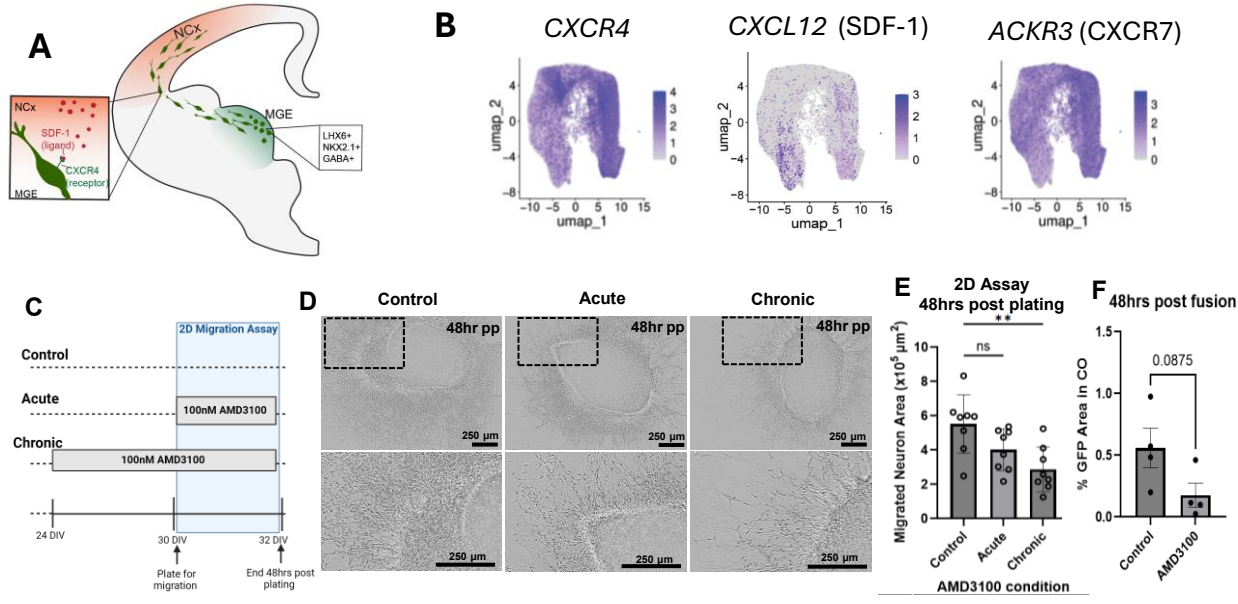

Supplemental Figure S5

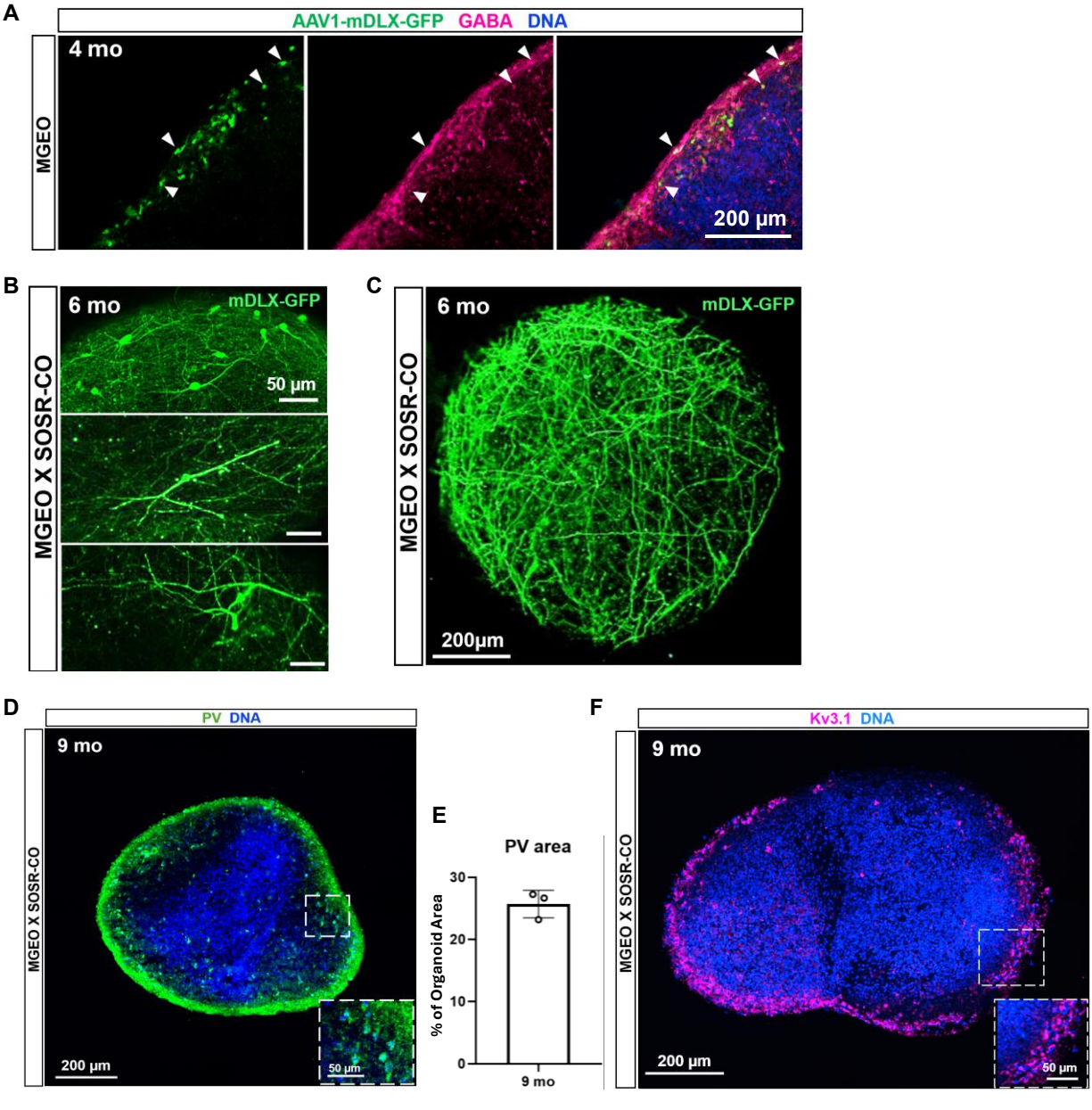

Supplemental Figure S6

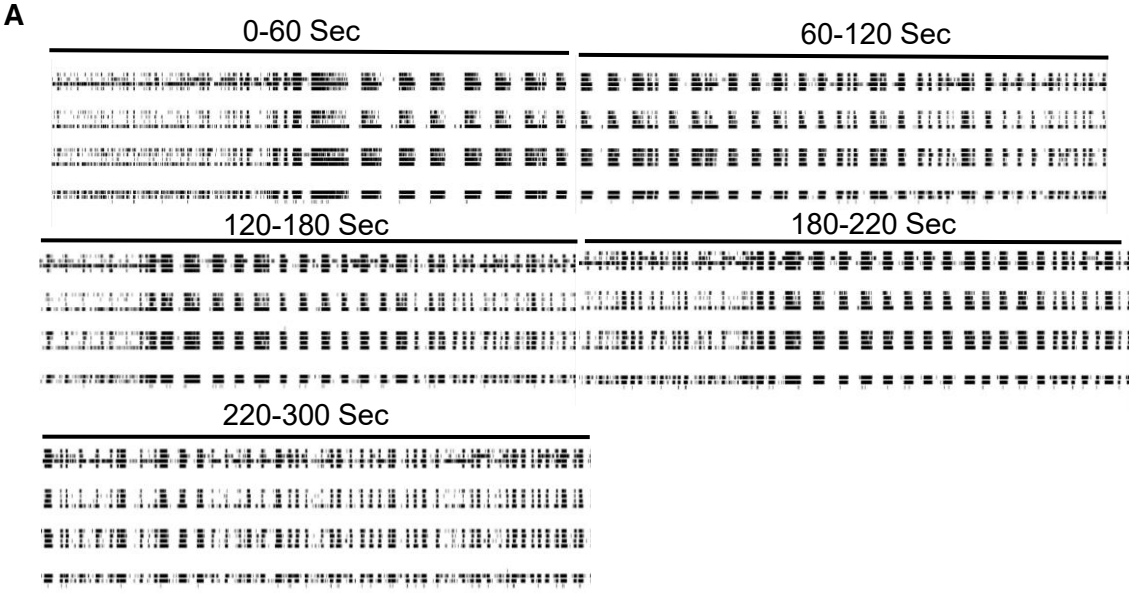

Supplemental Figure S7:
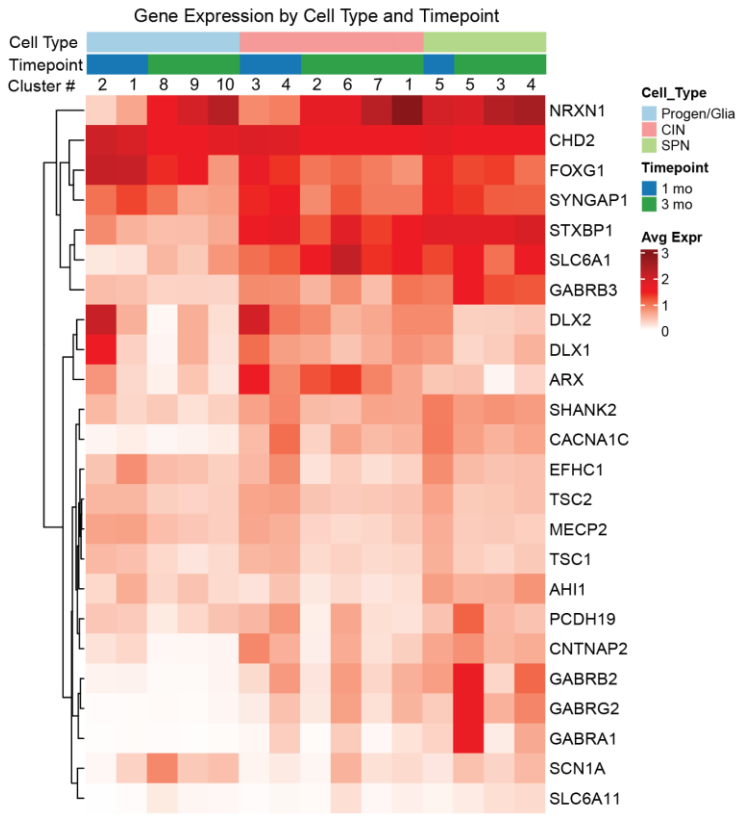
A